

Reminiscence of classical chaos in driven transmons

Joachim Cohen,^{1,*} Alexandru Petrescu,^{1,2,†} Ross Shillito,¹ and Alexandre Blais^{1,3}

¹*Institut Quantique and Département de Physique,
Université de Sherbrooke, Sherbrooke, Québec, J1K 2R1, Canada*

²*LPENS, Département de physique, Ecole normale supérieure,
Centre Automatique et Systèmes (CAS), MINES ParisTech,
Université PSL, Sorbonne Université, CNRS, Inria, 75005 Paris, France*

³*Canadian Institute for Advanced Research, Toronto, M5G1M1 Ontario, Canada*

(Dated: July 20, 2022)

Transmon qubits are ubiquitously used in quantum information processing architectures based on superconducting circuits. Because of their lifetime, strong drives are required to realize fast, high-fidelity, gates and measurements, including parametrically activated processes. Here, we show that even off-resonant drives, in regimes routinely used in experiments, can cause strong modifications to the structure of the transmon spectrum rendering a large part of it chaotic. Accounting for the full nonlinear dynamics in a Floquet-Markov formalism, we find that the coherence time of the computational states of transmons can be significantly altered in the presence of a chaotic layer. In particular, chaos-assisted quantum phase slips greatly enhance band dispersions. In the presence of a measurement resonator, we find that approaching chaotic behavior correlates with strong transmon-resonator hybridization, and an average resonator response centered on the bare resonator frequency. The phenomena described here should be present in all circuits based on low-impedance Josephson-junctions.

I. INTRODUCTION

Low-impedance Josephson junction circuits, where the Josephson energy dominates over the charging energy, are fundamental building blocks of superconducting quantum processors. Although the most widely used superconducting qubit is the transmon [1], capacitively shunted Josephson junctions appear in other species of qubits, such as the heavy fluxonium [2, 3], the $0 - \pi$ qubit [4] and the capacitively shunted flux qubit [5, 6]. Josephson junctions can also be used as simple nonlinear elements for parametrically activated multi-wave mixing [7–10], or as linear inductive elements in a Josephson junction array to realize superinductances [11, 12].

To meet the requirements of quantum information processing with fast and high-fidelity operations, strong driving fields that are off-resonant from the qubit are often used in parametrically activated coupling [7, 13], multi-qubit gates [14, 15] and dispersive readout [16]. However, off-resonant drives of even moderate amplitude are often observed to cause spurious qubit transitions [17–19]. This is the case of the dispersive readout whose quantum-non demolition (QND) character is observed only at very small drive amplitudes, corresponding to a few photons ($\bar{n} \sim 2$) populating the measurement resonator [17]. Models based on perturbative expansion in the qubit-resonator coupling [20] or in qubit anharmonicity and drive amplitude [20, 21] have been explored to understand the origin of these transitions. At large photon numbers ($\bar{n} \gtrsim 100$), qubit-resonator resonances [22] and

structural instabilities [13, 23] have been shown to result in spurious transitions. Recently, a numerical study of the full time dynamics of the transmon has shown that qubit-resonator resonances can lead to leakage of the transmon population to states lying above the Josephson junction cosine potential, something which has been referred to as ionization [24]. In that study, ionization was shown to coincide with the loss of QNDness experimentally observed at low photon numbers in Ref. [17].

Here, we show that the often-neglected highly excited states of the transmon can play an important role for current experimental parameters and drive amplitudes, even in the absence of ionization [13, 22, 25]. We find that a subset of the highly-excited states in the spectrum of a driven transmon, the so-called chaotic layer, significantly and unexpectedly dresses the charge dispersion of the low-energy transmon spectrum, with detrimental effects on the qubit dephasing time. This phenomenon can be understood as chaos-assisted [26] quantum phase slips [27]. The increased dependence on the offset charge even for the low-energy states suggests that, in the presence of strong drives, models that rely on a perturbed harmonic oscillator such as the Kerr nonlinear oscillator [28] cannot give an accurate description of the system, in particular because the selection rules derived from these models are no longer applicable [22]. In addition, we show that the chaotic layer makes steady-state populations deviate significantly from the Boltzmann distribution [23, 29, 30].

We draw upon the Floquet theory [29–31] of nonlinear oscillators [32] to distinguish between the chaotic and regular states [33, 34] of a driven transmon. We introduce a rescaling of the transmon Hamiltonian from which an effective Planck constant emerges, $\hbar_{\text{eff}} = \sqrt{8E_C/E_J}$ ($\hbar = 1$). In the transmon regime, where \hbar_{eff} is small, the chaotic dynamics of the classical driven transmon

* cohenj38@gmail.com

† alexandru.petrescu@mines-paristech.fr

becomes more resolved in the quantum spectrum as the number of chaotic states increases. In particular, we show that the spectrum of a single driven transmon is correlated [35]. In transmon systems, this type of analysis has been performed in the many-body regime [36]. Our study reveals that, within the range of current experimental parameters, the size of the classical chaotic domain is strongly sensitive to the drive frequency, something which can lead to instabilities in the quantum dynamics even at low drive power. Our results suggest ways to avoid experiments from being plagued by these instabilities.

Moreover, by simulating the full circuit QED model, we show that chaos develops along two directions, that of increasing resonator Fock state number and that of increasing drive power. In addition to validating the study of the single driven transmon, we show that the transmon and the resonator strongly hybridize in the chaotic phase. As a result, in the context of the dispersive readout where chaotic effects are close, spurious qubit transitions become possible.

The remainder of this article is organized as follows. In Sec. II, we introduce a rescaled version of the Hamiltonian along with the key parameters of the dynamics, we discuss chaos in the classical driven transmon, and briefly discuss the impact of classical chaos on the quantum system. Sec. III tackles the spectral properties of the system and the dependence of the instability on drive frequency. In Sec. IV, we consider the coupling of the transmon to a bath, and the impact of the chaotic layer on the coherence properties of the low-energy sector is analyzed. Sec. V focuses on the interplay of chaos and the validity of the dispersive approximation in the full circuit QED setup.

II. PERIODICALLY DRIVEN TRANSMON

The Hamiltonian of a transmon in a typical circuit QED setup takes the form [1, 37]

$$\mathbf{H}(t) = 4E_C(\mathbf{n} - n_g)^2 - E_J \cos(\phi) + \mathbf{nF}, \quad (1)$$

where \mathbf{n} and ϕ are respectively the charge and phase operators, E_C and E_J are the charging and Josephson energies, and n_g an offset charge. The phase ϕ is compact and takes its values in the range $[-\pi, \pi]$. The operator \mathbf{F} represents a classical driving field on the resonator or the coupling to a measurement resonator in a circuit QED setup [37]. As such, $\mathbf{F} = F_c(t) + \mathbf{F}_q$ can be expressed as the sum of a classical part and of a quantum part. The quantum part represents the displaced quadrature of the readout resonator, i.e. $\mathbf{F}_q = ig(\mathbf{a}^\dagger - \mathbf{a})$ where g is the light-matter coupling. On the other hand, the classical part is assumed to take the form $F_c(t) = \varepsilon_d \cos(\omega_d t)$ and represents either a direct capacitive drive on the transmon or the classical amplitude of the resonator field. In this work, we are concerned with the limit of strong drives,

where the classical part dominates over quantum fluctuations, i.e. $\varepsilon_d > g$. Expressing the drive amplitude $\varepsilon_d = 2g\sqrt{\bar{n}}$ in terms of an equivalent number of resonator photons \bar{n} , this strong drive limit corresponds to $\bar{n} > 1$. In typical cQED setup, one has $g/2\pi \sim 250\text{MHz}$ and $\bar{n} \geq 2$, resulting in an effective drive $\varepsilon_d/2\pi \geq 700\text{MHz}$.

In what follows, we neglect quantum fluctuations \mathbf{F}_q to study the periodically driven transmon Hamiltonian

$$\mathbf{H}(t) = 4E_C(\mathbf{n} - n_g)^2 - E_J \cos(\phi) + \varepsilon_d \cos(\omega_d t)\mathbf{n}. \quad (2)$$

We return to a full circuit QED model accounting for the presence of the resonator in Sec. V.

A. Classical model

We first consider the classical limit of the driven transmon Hamiltonian where we replace the conjugate operators $\{\phi, \mathbf{n}\}$ by the phase-space coordinates $\{\phi, n\}$. In doing so, it is useful to rescale energy and time using the relations $\tilde{H} = H/E_J$ and $\tilde{t} = \omega_p t$, where $\omega_p = \sqrt{8E_J E_C}/\hbar$ is the plasma frequency of the transmon. Under this transformation, which preserves Hamilton's equations, the classical Hamiltonian takes the form

$$\tilde{H}(\tilde{t}) = \frac{(\tilde{n} - \tilde{n}_g)^2}{2} - \cos \tilde{\phi} + \tilde{\varepsilon}_d \cos(\tilde{\omega}_d \tilde{t}) \tilde{n}. \quad (3)$$

This corresponds to the Hamiltonian of a driven charged classical pendulum with dimensionless momentum $\tilde{n} = zn$ and position $\tilde{\phi} = \phi$ [1]. Here, $z = \sqrt{8E_C/E_J}$ is the characteristic impedance of the transmon. In this rescaled form, the three relevant parameters of the classical driven transmon are the rescaled drive amplitude $\tilde{\varepsilon}_d = \varepsilon_d/\omega_p$, the rescaled drive frequency $\tilde{\omega}_d = \omega_d/\omega_p$ and the rescaled offset charge $\tilde{n}_g = z n_g$.

In the absence of a drive, two different types of motion of the system can be distinguished. For $\tilde{H} < 2$ (i.e. $H < 2E_J$), the system undergoes small and bounded phase oscillations. On the other hand, for $\tilde{H} > 2$, the system experiences unbounded full $\pm 2\pi$ rotations of the phase. While manipulations of the transmon qubit are designed such as to only lead to small phase oscillations, the transmon can be promoted to states above $2E_J$ by strong drives [13, 22–24]. In the quantum case, the resulting full rotations correspond to quantum phase slips [1, 27]. At the boundary of these two types of motion, defined by the trajectory of energy $\tilde{H} = 2$ also known as the separatrix, small perturbations can have a large impact, for example causing bounded oscillations to turn into unbounded rotations. This structural instability results in an irregular, chaotic, motion of the pendulum at finite drive amplitude in the vicinity of the separatrix [32].

A useful representation of the system dynamics, both regular and chaotic, is provided by the stroboscopic Poincaré sections obtained by plotting the value of the phase space coordinates $\{\tilde{\phi}(\tilde{t}), \tilde{n}(\tilde{t})\}$ at every period $\tilde{T} =$

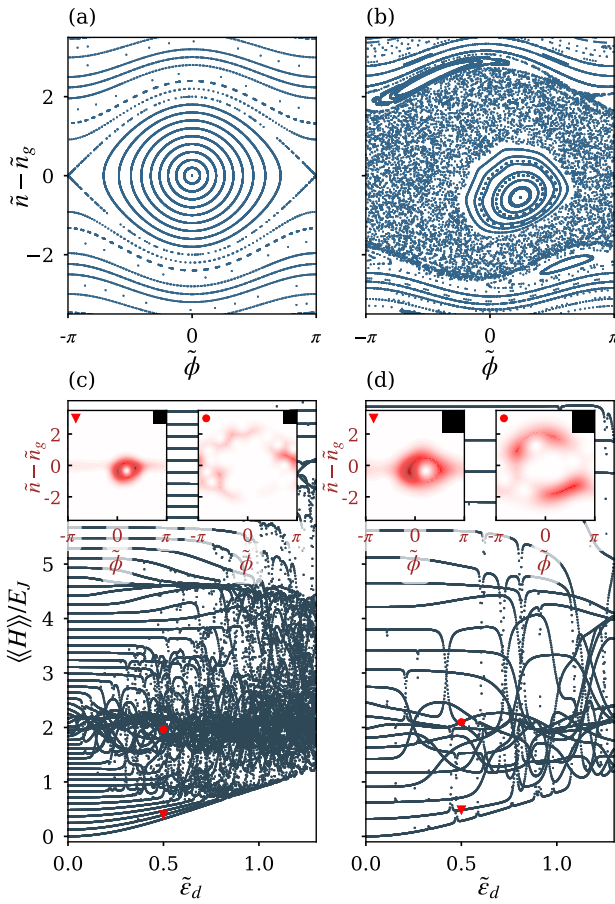


Figure 1. (a) Poincaré section of the undriven system and (b) of the system driven at $\tilde{\varepsilon}_d = 0.5$, $\tilde{\omega}_d = 1.34$ and with initial time $\tilde{T}/8$. In the driven case, a chaotic layer develops around the separatrix. Additional resonances within the unbounded states appear taking the form of tori located at the border of the separatrix. (c,d) Mean energy per cycle as a function of drive amplitude $\tilde{\varepsilon}_d$ for $\tilde{\omega}_d = 1.34$, $n_g = 0.25$, and for two different values of \hbar_{eff} : (c) $\hbar_{\text{eff}}^{-1} = 7.91$ ($E_J/E_C = 500$) and (d) $\hbar_{\text{eff}}^{-1} = 3$ ($E_J/E_C = 72$). In analogy to the classical case, strong hybridization of the states develops about the separatrix located at $\langle\langle H \rangle\rangle/E_J = 2$. The insets marked by a red triangle show the Husimi functions of the Floquet modes of the first excited state at $\tilde{\varepsilon}_d = 0.5$. Its wavefunction remains globally regular and is reminiscent of the first Fock state. The insets marked by a red dot correspond to a state located close to the separatrix. The corresponding Husimi function is irregular and delocalized over the corresponding classical chaotic domain in (b). The black squares represent the phase-space area \hbar_{eff} occupied by one state.

ω_p/ω_d of the drive for some initial condition [38]. Figure 1(a) first shows this in the absence of a drive. There, the two expected types of motions are clearly visible: the bounded oscillations leading to the closed orbits and the unbounded rotations to the nearly horizontal patterns. In the presence of the drive, see Fig. 1(b), the Poincaré sections break up into regular and chaotic re-

gions. The regular regions consist of weakly perturbed Kolmogorov-Arnold-Moser tori, reminiscent of the motion of the unperturbed system, while the chaotic region develops around the separatrix [32]. The small tori located within the regular unbounded trajectories in Fig. 1(b) are due to two resonances where the drive frequency $\pm\tilde{\omega}_d$ matches the energies of the trajectories which pass in the vicinity of $(\tilde{\phi}, \tilde{n}) = (0, \pm 2.5)$.

B. Quantum model

To compare the quantum dynamics to the classical one, we quantize the rescaled Hamiltonian of Eq. (3). Importantly, because the rescaling does not preserve the phase-space volume, it leads to a renormalization of the Planck constant upon quantization with $\hbar_{\text{eff}} = \hbar\omega_p/E_J = z$. As a result, the commutation relation of the rescaled operators is $[\tilde{\phi}, \tilde{n}] = i\hbar_{\text{eff}}$. Consequently, in addition to the three parameters that determine the classical dynamics enumerated above, $\tilde{\varepsilon}_d$, $\tilde{\omega}_d$, and \tilde{n}_g , the driven quantum dynamics of the transmon is characterized by a fourth parameter, \hbar_{eff} , characterizing quantum fluctuations.

The solutions to the time-dependent Schrödinger equation associated to the Hamiltonian in Eq. (2) are the time-dependent Floquet states $|\psi_k(t)\rangle = \exp(-i\varepsilon_k t)|\phi_k(t)\rangle$, characterized by the rescaled quasienergies $\tilde{\varepsilon}_k$ and the time-periodic Floquet modes $|\phi_k(t)\rangle$ [31].

The quasienergies of the Floquet modes are defined up to integer multiples of the drive frequencies, and hence are not indicative of the amount of energy stored in the system. However, the mean energy per cycle for mode $|\phi_k(t)\rangle$ can be defined as [39]

$$\langle\langle H \rangle\rangle = \frac{1}{T} \int_0^T dt \langle \phi_k(t) | \mathbf{H}(t) | \phi_k(t) \rangle, \quad (4)$$

where T is the period of the drive. This mean energy per cycle is plotted in Fig. 1(c) as a function of the drive amplitude $\tilde{\varepsilon}_d$ and different Floquet states k for a very weakly nonlinear transmon qubit with $\hbar_{\text{eff}}^{-1} = 7.91$ ($E_J/E_C = 500$). As the drive amplitude increases, the perturbation hybridized the states around the energy $\langle\langle H \rangle\rangle/E_J = 2$, corresponding to the energy of the separatrix in the classical system, and does so in an increasingly large bandwidth around that energy. Remarkably the main features subexist in the more experimentally relevant case of $\hbar_{\text{eff}}^{-1} = 3$ ($E_J/E_C = 72$), although the hybridization is visually less pronounced because the level separations are larger, see Fig. 1(d).

The diffusion of classical trajectories through the chaotic domain translates to delocalized Husimi functions of the Floquet modes for the driven quantum system [30, 40]. This can be intuitively understood by the fact that the Floquet modes are eigenstates of the propagator over one period of the drive, which is the quantum analog of the stroboscopic Poincaré map defined above [41]. In the insets of Fig. 1(c) and Fig. 1(d), we

plot the Husimi functions at time $T/8$ of the Floquet modes indicated by the red markers on the spectra at $\tilde{\varepsilon}_d = 0.5$. Because the phase is defined on $[-\pi, \pi]$, we use the definition for a coherent state on a circle of Ref. [42]. The insets indicated by the red triangle corresponds to the Husimi functions of the Floquet modes of the first excited state. Because it is outside of the region where the states are strongly mixed (i.e. outside of the chaotic layer in the classical system), its wavefunction remains globally regular and is reminiscent of the first Fock state. On the other hand, the insets marked by a red dot correspond to a state located close to the separatrix. The corresponding Husimi functions are irregular and delocalized over the region corresponding to the chaotic layer in the classical case, see Fig. 1(b). The black squares in the upper right corner of the insets indicate the phase space area \hbar_{eff} occupied by one state. A smaller \hbar_{eff} results in a smaller amplitude of quantum fluctuations, and therefore in more resolved features in the Husimi functions.

III. QUANTUM SIGNATURES OF CHAOS IN THE DRIVEN SPECTRUM

A. Level-spacing statistics

The chaotic nature of the states near the separatrix can be confirmed through the correlated nature of the Floquet spectrum, which is manifest in the distribution of level spacings $P(\Delta)$. Indeed, the strong level hybridization observed near the separatrix results in level repulsion and, in turn, to a Floquet spectrum with strong correlations in the distribution of the spacing between levels. In that situation, $P(\Delta)$ is expected to follow the Wigner-Dyson distribution (full line in Fig. 2) [35]. In contrast, in the regular regime levels are uncorrelated and their distribution is Poissonian, as is characteristic of random uncorrelated events (dashed line in Fig. 2) [35].

To display this distribution, we consider a set of N states with sorted quasienergies $\varepsilon_1 \leq \dots \leq \varepsilon_N$ lying within the first Brillouin zone, i.e. $|\varepsilon_n| \leq \omega_d/2$ for all n . The spacing between adjacent quasienergy levels is defined by $\Delta_n = (\varepsilon_{n+1} - \varepsilon_n)/\bar{\Delta}$ for $n = 1, \dots, N-1$, where $\bar{\Delta} = \omega_d/N$ is the mean level spacing. We also define $\Delta_N = (\varepsilon_0 - \varepsilon_N + \omega_d)/\bar{\Delta}$ at the boundary of the Brillouin zone. In the limit of large N , the distribution $P(\Delta)$ is expected to follow the Wigner-Dyson statistics for correlated spectrum [43], whereas it is expected to follow a Poisson distribution for an uncorrelated spectrum.

In analogy with the study of classical chaos, we define the chaotic domain using the mean energy per cycle $\langle\langle H \rangle\rangle$. As can first be seen in Fig. 1(c) for $\hbar_{\text{eff}}^{-1} = 7.91$, the mean energies of the chaotic states are concentrated around $2E_J$, and are separated from the regular states by a gap. The relevant energy bandwidth of the chaotic zone depends on the drive amplitude and, for $\tilde{\varepsilon}_d = 0.5$, here we take the N states whose energies satisfy $1.6 < \langle\langle H \rangle\rangle/E_J < 2.5$. For the value of $\hbar_{\text{eff}}^{-1} = 3$ correspond-

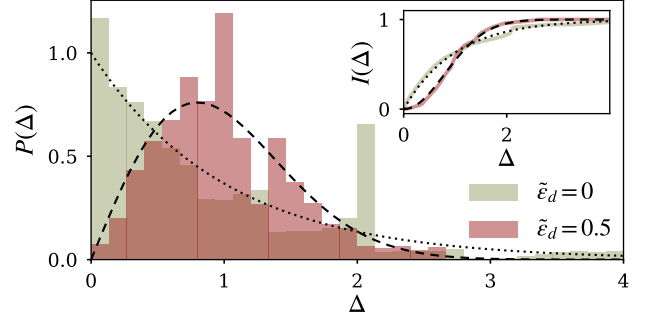


Figure 2. Level spacing statistics for $\hbar_{\text{eff}}^{-1} = 3$ and $\tilde{\omega}_d = 1.34$ for the undriven (green) and driven (red) spectrum. The set of states comprises those of mean energy satisfying $1.6 < \langle\langle H \rangle\rangle/E_J < 2.5$. The statistics is generated using the Floquet spectra corresponding to 200 values of n_g uniformly distributed over the interval $[0, 0.5]$. The driven spectrum distribution follows the Wigner-Dyson distribution (dashed line), while the distribution of energies for the undriven system follows the Poisson distribution (dotted line). The inset shows the integrated distribution $I(\Delta) = \int_0^\Delta d\Delta P(s)$.

ing to a typical transmon qubit the spectrum, however, displays only a handful of chaotic states in this energy bandwidth. With about $N \sim 7$ levels, see Fig. 1(d), this is far from enough to generate meaningful level-spacing statistics. To circumvent this problem, we use the offset charge n_g uniformly distributed in the interval $[0, 0.5]$ to generate statistics. This is possible because, even in the transmon regime, the chaotic states are not confined in the cosine potential well making them very sensitive to the offset charge. We return in Sec. IV to some of the observable implications of this n_g dependence of the chaotic states.

We plot in Fig. 2 the cumulative histograms of $P(\Delta)$ obtained from adding the distributions corresponding to 200 values of n_g uniformly distributed in the interval $[0, 0.5]$ for $\tilde{\varepsilon}_d = 0$ (green bars) and $\tilde{\varepsilon}_d = 0.5$ (red bars). In the absence of a drive, the system is regular and $P(\Delta)$ follows the Poisson distribution expected for an uncorrelated spectrum. This also suggests that the undriven spectrum is well randomized by the variation of n_g . In contrast, at $\tilde{\varepsilon}_d = 0.5$, $P(\Delta)$ approaches the Wigner-Dyson distribution. The number of states N in the selected energy bandwidth has increased in the chaotic case. This is due to the hybridization of states with mean energy close to the separatrix region $\langle\langle H \rangle\rangle \sim 2E_J$, as mentioned above. More generally, the extent of the chaotic layer is seen to increase with the drive amplitude, something which is particularly clear in Fig. 1(c). The inset of Fig. 2 shows the integrated distribution $I(\Delta) = \int_0^\Delta d\Delta P(s)$ for which the statistical variations are reduced because of the integration, thereby allowing for a clearer distinction between uncorrelated and correlated spectra [35].

In summary, the eigenstates of the system divide the Hilbert space into roughly 3 subspaces: the regular low-

energy phase-like states, the chaotic states, and the regular charge-like states.

B. Drive frequency dependence

In addition to spreading over an increasingly large energy bandwidth with increasing drive amplitude, the size of the chaotic region also strongly depends on the drive frequency. This is illustrated in Fig. 3(a)-(d) which shows the Poincaré sections for $\tilde{\omega}_d = 0.75, 1.25, 2.25$ and 4.25 . The mean energy spectra of the corresponding quantum systems are shown in Fig. 3(e)-(h) as a function of $\tilde{\epsilon}_d/\tilde{\omega}_d$ for $\hbar_{\text{eff}}^{-1} = 2.45$ and $n_g = 0.25$. To compare the effect of different drive frequencies, the ac-Stark shift computed from the quasienergies of the ground and first excited states is fixed to 100 MHz in panels (a)-(d) (see Appendix A). The corresponding drive amplitudes are represented by a vertical black dashed line in Fig. 3(e)-(h). In panels (a)-(d), the width of the chaotic layer is observed to be maximal for intermediate drive frequencies $\tilde{\omega}_d \sim 1 - 2$. This observation is in qualitative agreement with approximate the expression for the width of the chaotic layer around the separatrix

$$W_c/E_J \approx \tilde{\epsilon}_d \tilde{\omega}_d \operatorname{sech}\left(\frac{\pi \tilde{\omega}_d}{2}\right), \quad (5)$$

a result which is valid for $\tilde{\omega}_d > 1$ [38, 44]. Following this expression, the chaotic layer is expected to have a maximal width for $1 < \tilde{\omega}_d < 2$, and to exponentially decrease in width with increasing $\tilde{\omega}_d$ for $\tilde{\omega}_d > 2$.

The approximate expression for the width, however, does not account for resonances that result in the additional tori observed in Fig. 3(a)-(d). In particular, in the range $0.6 \lesssim \tilde{\omega}_d \lesssim 3$, which includes the regime of operation of current experiments, we find that resonances play an essential role in drive-induced instabilities. The origin of these resonances can be qualitatively understood by expressing the classical Hamiltonian of Eq. (3) in the equivalent form

$$\tilde{H}(\tilde{t}) = \frac{(\tilde{n} - \tilde{n}_g)^2}{2} - \cos\left[\tilde{\phi} + \frac{\tilde{\epsilon}_d}{\tilde{\omega}_d} \sin(\tilde{\omega}_d \tilde{t})\right]. \quad (6)$$

Using the Jacobi-Anger expansion to first order in $\tilde{\epsilon}_d/\tilde{\omega}_d$, this can be approximated as

$$\begin{aligned} \tilde{H}(\tilde{t}) \approx & \frac{(\tilde{n} - \tilde{n}_g)^2}{2} - J_0\left(\frac{\tilde{\epsilon}_d}{\tilde{\omega}_d}\right) \cos \tilde{\phi} \\ & + J_1\left(\frac{\tilde{\epsilon}_d}{\tilde{\omega}_d}\right) [\cos(\tilde{\phi} - \tilde{\omega}_d \tilde{t}) - \cos(\tilde{\phi} + \tilde{\omega}_d \tilde{t})], \end{aligned} \quad (7)$$

where $J_k(z)$ is the k -th Bessel functions of the first kind. The first line, $\tilde{H}_{\tilde{\epsilon}_d} = (\tilde{n} - \tilde{n}_g)^2/2 - J_0(\tilde{\epsilon}_d/\tilde{\omega}_d) \cos \tilde{\phi}$, describes an undriven pendulum with a potential energy reduced by the factor $J_0(\tilde{\epsilon}_d/\tilde{\omega}_d)$. The second line is of smaller amplitudes and describes the first harmonic of the time-dependent perturbation. Higher-order harmonics of

the drive are neglected because their amplitude is suppressed by the factor $J_k(\tilde{\epsilon}_d/\tilde{\omega}_d)$ and because the corresponding resonances occur at higher frequency, $\tilde{\omega} > 2\tilde{\omega}_d$. The effects of the perturbation can be understood by inserting the solution $(\tilde{\phi}(t), \tilde{n}(t))$ of the system ruled by the time-independent Hamiltonian $\tilde{H}_{\tilde{\epsilon}_d}$ with initial conditions $(\tilde{\phi}_0, \tilde{n}_0)$. Depending on the drive frequency, resonances can occur either within the bounded states or the unbounded states.

The trajectories representing the bounded states of the pendulum can be generated in the Poincaré sections with the initial conditions $(\tilde{\phi}_0 < \pi, \tilde{n}_0 = 0)$. For small oscillations, the pendulum behaves as a slightly anharmonic oscillator, and its oscillation frequency decreases as the oscillation amplitude $\tilde{\phi}_0$ increases. For $|\tilde{\phi}_0| < 0.8\pi$, the nonlinearity does not play an important role and the pendulum frequency varies smoothly. This corresponds to a frequency range $0.65 \lesssim \tilde{\omega} < 1$ for the pendulum oscillation. In this case, under $\tilde{H}_{\tilde{\epsilon}_d}$ the trajectory that passes through $(\tilde{\phi}_0, 0)$ takes the standard form $\tilde{\phi}(t) \approx \tilde{\phi}_0 \sin(\tilde{\omega}t)$ where we have neglected the higher harmonics of the motion. Inserting this expression for $\tilde{\phi}$ in the second line of Eq. (7) leads to the slowly rotating terms $J_1(\tilde{\epsilon}_d/\tilde{\omega}_d) J_{2k+1}(\tilde{\phi}_0) \cos[(\tilde{\omega}_d - (2k+1)\tilde{\omega})\tilde{t}]$.

The case $k = 0$ corresponds to a 1:1 resonance, i.e. $\tilde{\omega}_d = \tilde{\omega} \in [0.65, 1]$, which strongly impacts the low-energy states of the system. At $\tilde{\omega}_d = 0.75$ it appears as a second set of tori located close to the central tori, see the red-coloured region in Fig. 3(a). Large instability results from the overlap between these two tori, with a chaotic layer arising at their separatrices [32]. The resulting increased width of the chaotic layer is not captured by the approximate expression of Eq. (5). The case $k = 1$ leads to a 1:3 resonance for $\tilde{\omega}_d = 3\tilde{\omega} \in [2, 3]$. For $\tilde{\omega}_d = 2.25$ this resonance results in 3 sets of tori surrounding the central regular island, see the three green-colored regions in Fig. 3(c)]. Although of smaller amplitudes than the 1:1 resonance, the overlap of this resonance with the main set of tori is likely to produce unstable motion at the boundary of these. Note also the appearance of a weak 1:5 resonance at $\tilde{\omega}_d = 4.25$ resulting in 5 small tori within the regular island, see the green-colored region in Fig. 3(d).

In contrast, no direct resonance occurs for the case $1.1 < \tilde{\omega}_d < 1.5$ which is common for the dispersive readout, see Fig. 3(b) for $\tilde{\omega}_d = 1.25$. Nevertheless, as expected from Eq. (5), the width of the chaotic layer is large at this drive frequency.

In the quantum case, the resulting large chaotic layer translates into a large hybridization of the states even at low drive amplitude, see the mean energy spectra Fig. 3(e-g). This hybridization can be further observed from the modification of the rate matrices (see Appendix A). This state hybridization can lead to loss of the QND character of the dispersive readout. As a concrete example, the value of \hbar_{eff}^{-1} and $\tilde{\omega}_d = 0.75$ of Fig. 3(f) was chosen to match the experimental parameters of Walter *et al.* [25] where the dispersive readout

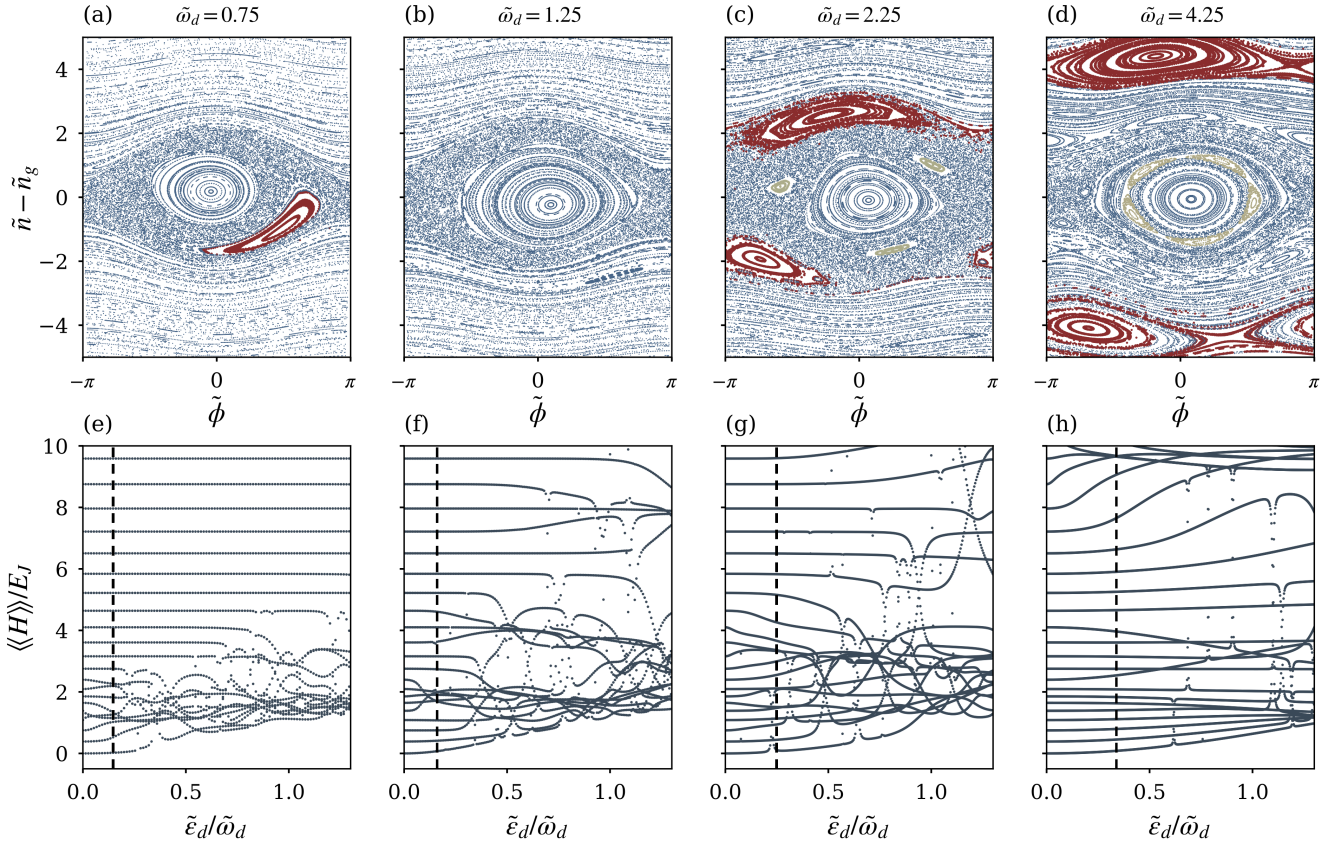


Figure 3. (a)-(d): Poincaré sections at time $T/8$ for the drive frequencies (a) $\tilde{\omega}_d = 0.75$, (b) $\tilde{\omega}_d = 1.25$, (c) $\tilde{\omega}_d = 2.25$ and (d) $\tilde{\omega}_d = 4.25$. The drive amplitudes are chosen such that the frequency of the $0 - 1$ transition in the quantum system is ac-Stark shifted by 100 MHz for all $\tilde{\omega}_d$. (e)-(f): Mean energy spectra as a function of $\tilde{\varepsilon}_d/\tilde{\omega}_d$ at the same respective drive frequencies, with $\hbar_{\text{eff}}^{-1} = 2.45$ and $n_g = 0.25$. In each case, the drive amplitude yielding an ac-Stark shift of 100 MHz is indicated by the vertical black dashed line – the above Poincaré sections have been computed for these amplitudes. For the parameters of panels (a), (c) and (d), a 1:1 resonance occurs between the drive and the system. In (a), this resonance results in a second set of tori within the bounded states of the system (red region). The overlap of the small oscillation and this resonance results in a large chaotic layer. In the quantum system (e), this leads to strong level hybridization. In panels (c) and (d), the drive comes in resonance with the unbounded states, resulting in two additional out-of-phase sets of tori rather than one (red regions). From (c) to (d), these tori move away from the center as the drive frequency increases. In (c) and (d), 1:3 and 1:5 resonances emerge (green region). In (c), the proximity of the 1:1 (red) and 1:3 (green) resonances to the regular island also causes large instabilities, both in the classical and quantum systems. In (d), the resonances are far and the width of the chaotic layer is smaller, as expected from Eq. (5). In (b), the resonance is absent.

fidelity was observed to degrade for measurement photon numbers $\bar{n} > 2.5$, something which was attributed to measurement-induced mixing of unknown origin. Using the light-matter coupling of $g/2\pi = 208$ MHz reported in Ref. [25], $\bar{n} = 2.5$ can be converted to an effective drive $\tilde{\varepsilon}_d = 0.105$ on the transmon. As can be observed in Fig. 3(e), the first excited state is “absorbed” in the chaotic layer for $\varepsilon_d \gtrsim 0.1$. Since chaotic states often lead to strong hybridization between the transmon and the readout resonator (see Sec. V), this hints at chaos-induced state mixing and non quantum-demolition effects in the readout beyond that drive amplitude. Although the above mean field analysis can qualitatively predict unstable behavior of the transmon, the agreement can-

not be expected to be quantitative at low resonator photon numbers since vacuum fluctuations of the resonator field and qubit-resonator parametric processes occurring in the presence of a readout tone can play an important role. We address some of these mechanisms in Sec. V.

The drive can also come in resonance with unbounded states of the pendulum with energy $\tilde{H}_{\tilde{\varepsilon}_d} > 2J_0(\tilde{\varepsilon}_d/\tilde{\omega}_d) \sim 2$. The trajectories at those energies take the approximate form $\tilde{\phi}(\tilde{t}) = \pm\tilde{\omega}\tilde{t} + F(\tilde{t})$, where F is a function of period $2\pi/\tilde{\omega}$ [32]. Using this expression in Hamilton’s equation of motion for the phase, we find that the oscillation frequency satisfies $\tilde{\omega} = |\langle\langle \tilde{n} - \tilde{n}_g \rangle\rangle| \gtrsim 1.5$, where $|\langle\langle \tilde{n} - \tilde{n}_g \rangle\rangle|$ is the averaged momentum of the trajectory over one period. This lower bound can vary with the

drive amplitude through the effect of the reduction factor $J_0(\tilde{\varepsilon}_d/\tilde{\omega}_d)$. To leading order, substituting this expression for $\tilde{\phi}$ in the second line of Eq. (7) results in the term $A_0 J_1(\tilde{\varepsilon}_d/\tilde{\omega}_d) \cos[\pm(\tilde{\omega} - \tilde{\omega}_d)\tilde{t}]$, where A_0 is the zeroth Fourier component of $\cos[F(\tilde{t})]$. Hence, for $\tilde{\omega}_d = \tilde{\omega} \gtrsim 1.5$, this resonance appears in the form of two tori moving clockwise and anti-clockwise, corresponding to $\pm\omega_d$, as depicted by the red-coloured regions in Fig. 3(c) for $\tilde{\omega}_d = 2.25$ and Fig. 3(d) for $\tilde{\omega}_d = 4.25$. At $\tilde{\omega}_d = 2.25$, the proximity of the resonance with the regular island results in a large chaotic domain which translates in strong state hybridization in the quantum case, see Fig. 3(g). Because the average momentum associated to this resonance is $|\langle \tilde{n} - \tilde{n}_g \rangle| = \tilde{\omega}_d$, the pairs of tori are further away from the center of phase space with increasing drive frequency. For this reason, at $\tilde{\omega}_d = 4.25$, this resonance is far from the separatrix of the undriven system and does not affect the chaotic layer. As a result, for $\tilde{\omega}_d = 4.25$ and at larger drive frequencies, the width of the chaotic layer is exponentially suppressed as expected from Eq. (5). In this situation, the absence of instability yields a mean energy spectrum with little state hybridization, see Fig. 3(h).

To summarize the above, the frequency ranges $0.65 < \tilde{\omega}_d < 1$ and $1.5 \leq \tilde{\omega}_d \leq 3$ lead to strong instabilities, in particular for the former. The parameter regime $1.1 < \tilde{\omega}_d < 1.5$ avoids resonances but has a large chaotic layer around the separatrix. For $\tilde{\omega}_d \geq 3.5$, resonances do not affect the bounded states (or very weakly through resonances of order greater than 5), and the width of the chaotic layer is suppressed. As shown in the next sections, the presence of the chaotic layer impacts the coherence times of the transmon qubit, and it should therefore be minimized when operating the transmon with strong drive, e.g. in dispersive qubit readout. The frequency ranges $1.1 \leq \tilde{\omega}_d \leq 1.5$ and $\tilde{\omega}_d \geq 3.5$ seem to be more benign.

IV. IMPACT ON COHERENCE PROPERTIES

Having established that the driven capacitively shunted Josephson junction exhibits signatures of chaos even at the large \hbar_{eff} corresponding to the transmon regime, we now turn to the impacts of this observation on coherence properties of the transmon in the presence of a bosonic bath. In this situation, the total Hamiltonian now takes the form

$$\mathbf{H}(t) = 4E_C(\mathbf{n} - n_g)^2 - E_J \cos(\phi) + \varepsilon_d \cos(\omega_d t) \mathbf{n} + i \mathbf{n} \sum_k g_k (\mathbf{b}_k^\dagger - \mathbf{b}_k) + \sum_k \omega_k \mathbf{b}_k^\dagger \mathbf{b}_k, \quad (8)$$

where \mathbf{b}_k and \mathbf{b}_k^\dagger are the annihilation and creation operators of the bath modes. Because of hybridization with states in the chaotic layer which have a strong charge dispersion, it is important to keep the gate charge n_g in Eq. (8) even when interested in the coherence properties of the low-lying eigenstates of the system.

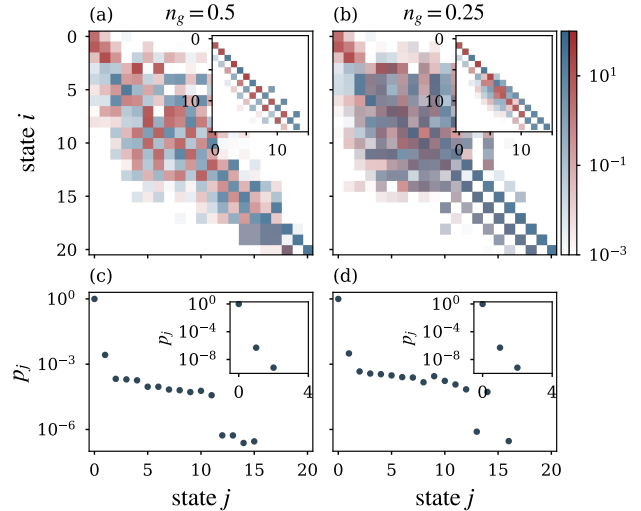


Figure 4. Top panels : Rate matrices in units of the coupling strength to the bath, at $\tilde{\epsilon}_d = 0.4$, $h_{\text{eff}}^{-1} = 3$, $\tilde{\omega}_d = 1.34$ and $T = 10$ mK for (a) $n_g = 0.5$ and (b) $n_g = 0.25$. The states are sorted by their mean energy $\langle\langle H \rangle\rangle$. The blue (red) squares correspond to the sum of rates involving an even (odd) number of drive photons k . The insets show the rate matrices of the undriven systems. At finite drive, the instability develops around the separatrix leading to an irregular block in the rate matrix also allowing for upward excitation rates. At the symmetric point $n_g = 0.5$, the red and blue squares do not overlap, while at $n_g = 0.25$, hybridization of parity sectors can be observed through the presence of purple squares even in the low-energy sector. The purple squares in (a) are due to numerical errors (see text). Bottom panels : Steady-state population as derived from the above rate matrices for (c) $n_g = 0.5$ and (d) $n_g = 0.25$. In the driven system, a plateau forms over the states that are part of the chaotic block of the rate matrices, instead of the regular exponential distribution in the undriven case, as shown in the insets.

A. Rate matrix and steady-state population

Within the Floquet-Markov description of the system-bath coupling, the bath-induced transition rate from Floquet state j to i , is given by [31]

$$\Gamma_{ij} = \sum_k |n_{ijk}|^2 [\Theta(\Delta_{ijk}) + n_B(|\Delta_{ijk}|)] J(|\Delta_{ijk}|), \quad (9)$$

where $\Theta(x)$ denotes the Heaviside function, $n_B(x)$ is the thermal occupation number of the bath, and $\Delta_{ijk} = \varepsilon_j - \varepsilon_i - k\omega_d$. The spectral function $J(x)$ is assumed to be that of an ohmic bath, i.e. $J(x) \propto x \exp(-|x|/\omega_c)$, where ω_c is a high-frequency cut-off. In the expression for Γ_{ij} , k can be interpreted as the number of drive photons participating positively or negatively to the transition. We have also introduced the charge operator matrix elements

$$n_{ijk} = \frac{\omega_d}{2\pi} \int_0^{2\pi/\omega_d} dt \langle \phi_i(t) | \mathbf{n} | \phi_j(t) \rangle \exp(i\Delta_{ijk}t), \quad (10)$$

where $|\phi_j(t)\rangle$ are the Floquet modes of the driven system.

The rate matrices of the driven transmon at $\tilde{\varepsilon}_d = 0.4$ and a temperature of $T = 10$ mK are shown for $n_g = 0.5$ in Fig. 4(a) and for $n_g = 0.25$ in Fig. 4(b). As a comparison, the insets show the rate matrices in the undriven case. For a given transition Γ_{ij} , the blue (red) squares sum the contributions from even (odd) values of k , with purple squares indicating contributions from both even and odd values. At zero drive, the upper triangular sector of the rate matrices (corresponding to upward transitions) contains negligible but non-zero elements due to the finite temperature (not visible in the insets). At finite drive, the instability develops around the states located on the separatrix (typically around the 8th excited state), forming an irregular block in the rate matrix. In particular, states within the chaotic layer are all coupled to one another through the charge operator. In addition, because of the drive photons, upward transitions are now apparent.

In the transmon regime, the low-energy sector is almost independent of the offset charge and, if one neglects its influence, the Hamiltonian becomes effectively symmetric under the parity transformation $\phi \rightarrow -\phi$ (and $\mathbf{n} \rightarrow -\mathbf{n}$) (see Appendix B). Because it neglects the gate charge, this symmetry is implicit in the Kerr nonlinear oscillator model of the transmon. Although this symmetry is exact only at $n_g = 0$ and $n_g = 0.5$, at zero drive it results in a suppression of the matrix elements of the charge operator $n_{i,i+2}$ in the low-energy sectors for both $n_g = 0.5$ and $n_g = 0.25$, and forbids the transition $i \rightarrow i + 2$, see insets of Fig. 4(a,b). The fact that this is only an approximate symmetry at $n_g = 0.25$ is apparent for the states in the separatrix region and above.

In the presence of a drive term $\varepsilon_d \cos(\omega_d t)\mathbf{n}$, the inversion symmetry only holds together with the time translation $t \rightarrow t + \pi/\omega_d$ [31]. This symmetry of the driven Hamiltonian defines even and odd parity sectors among the time-dependent Floquet states (see Appendix B). Because the charge operator is anti-symmetric, under this generalized parity symmetry, transitions through the charge operator between two states of the same (opposite) parity can only involve an odd (even) number of drive photons k . As can be seen in Fig. 4(a) for $n_g = 0.5$, blue and red squares do not mix (i.e. there are no purple squares) indicating that the symmetry is respected for that gate charge. The purple squares appearing for states 18 and 19 only result from precision errors. The situation is very different at $n_g = 0.25$, where purple squares appear in the chaotic layer but also for transitions involving the low-energy states. This results in transitions that are otherwise forbidden at the symmetric points $n_g = 0$ and $n_g = 0.5$. As discussed in further details in the next section, the breaking of this effective symmetry in the low-energy sector is a consequence of a strong increase of the band dispersion in the presence of drive. Interestingly, transition forbidden by the apparent inversion symmetry of the transmon were experimentally observed under strong drives, but remained unexplained [22].

Finally, the rate matrix can be used to compute the

system's steady-state density matrix ρ_{ss} . Under the assumption of weak system-bath coupling, the steady state is diagonal in the Floquet basis

$$\rho_{ss}(t) = \sum_j p_j |\phi_j(t)\rangle \langle \phi_j(t)|, \quad (11)$$

where the populations p_j satisfy the rate equations $p_j = \sum_i \Gamma_{ji} p_i - \sum_i \Gamma_{ij} p_j$. The insets of Fig. 4(d) and Fig. 4(d) show these steady-state populations for the undriven systems for $\hbar_{\text{eff}}^{-1} = 3$ which is typical of the transmon regime. As expected, the populations follow the thermal distribution with populations quickly dropping below 10^{-10} . In contrast, in the driven systems (here with $\tilde{\varepsilon}_d = 0.4$), the steady-state populations form a plateau corresponding to the chaotic layer. This behavior is typical of chaotic systems [29, 30]. Increasing the drive amplitude, the chaotic layer and therefore the plateau grow, until all the low-energy states are part of the plateau, including the ground state. This results in a dramatic decrease of the purity of the transmon's steady state, an observation which is in agreement with numerical [23] and experimental results [13].

This discussion sheds light on the distinction between the time-dynamics of the transmon ionization numerically observed in [24], and the ionization in the steady state [13, 23]. In the former, one captures the dynamics of the dispersive readout of a transmon qubit at high drive power. As the cavity rings up on the scale of κ^{-1} , where κ is the photon loss rate, the effective field amplitude ε_d on the transmon increases. Starting in the ground or first excited states, the system follows the corresponding first or second line in the mean energy spectrum of Fig. 1(c). Ionization occurs when one of those lines crosses a large resonance with a chaotic state, i.e. when the mean energy suddenly increases in Fig. 1(c), something which happens at $\tilde{\varepsilon}_d \approx 1.1$ for the ground state and at $\tilde{\varepsilon}_d \approx 0.75$ for the first excited state. Once a chaotic state is populated, it naturally decays due to its numerous transition rates to many states. On the other hand, ionization in the steady state is only a function of the rate matrix, which in turn depends on the matrix elements of the charge operator in the Floquet basis. Large matrix elements between the ground state and the chaotic states are likely to lead to ionization through bath-induced transitions. Although a resonance leads to matrix elements, the contrary is not necessarily true.

B. Chaos-assisted tunneling : effects on T2

A defining feature of the transmon is its charge dispersion which is exponentially suppressed with $8\hbar_{\text{eff}}^{-1} = \sqrt{8E_J/E_C}$, making it almost insensitive to charge noise [1]. Here, we show that this exponential suppression does not necessarily hold in the presence of a periodic drive.

In the previous section, we have seen that the Hamiltonian of the driven transmon can be approximately di-

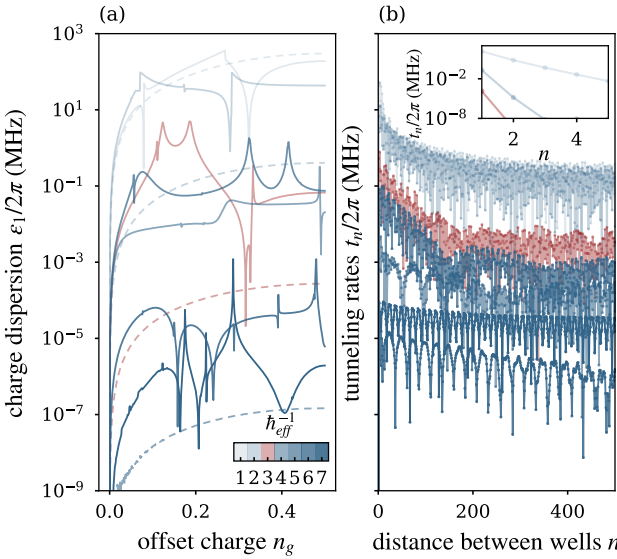


Figure 5. (a) Band dispersion of the first excited state for the undriven (dashed lines) and driven (solid lines) transmon with $\tilde{\varepsilon}_d = 0.4$, for $\hbar_{\text{eff}}^{-1} = \sqrt{E_J/8E_C}$ in the range [1, 7]. The experimentally relevant value of $\hbar_{\text{eff}}^{-1} = 3$ is highlighted in red. The exponential suppression of the dispersion of the undriven case is strongly modified by the presence of the drive, showing both an overall increase and sharp features. The latter are due to small resonances with chaotic states that have a large charge dispersion. (b) Fourier coefficients of the energy $\varepsilon_1(n_g)$ of the first excited state at finite drive amplitude $\tilde{\varepsilon}_d = 0.4$ as a function of the Fourier index n . These Fourier components are understood as phase-slip rates of order n . The spikes or ‘‘abrupt’’ resonances in (a) are responsible for the slowly decaying tail in (b) that translates to long-range tunneling between the Josephson potential wells. The inset shows the tunneling rates of the undriven systems with the expected exponential suppression with the distance between wells.

vided into regular blocks of states, phase-like and charge-like states, on which the drive acts perturbatively, and one chaotic block with a strongly correlated spectrum. From perturbation theory performed on the regular block, one would expect a drive to lead to a slow hybridization of regular low-lying states. In this situation, the ground and first excited states would therefore weakly inherit an offset-charge sensitivity from weak dressing with higher energy states, leading to an overall small increase of the band dispersion with the drive amplitude. In practice, we find that the presence of the chaotic layer results in the energy dispersion of these states to be significantly modified when the system is driven. This is illustrated by the solid lines in Fig. 5(a) for the first excited state of the transmon with values of \hbar_{eff} in the range 1 to 7 as labeled by the different colors. As a comparison, the dashed lines correspond to the undriven transmon and for which the exponential suppression of the charge dispersion is clearly observed. In contrast, in the driven transmon the energy bands are disrupted by peaks of multiple orders of magni-

tude in addition to being, on average, substantially larger than in the undriven case. The sharpness of these peaks is indicative of a weak resonance between the first excited state and strongly n_g -dependent states located in the chaotic layer. These results are obtained by identifying the first excited states by tracking the Floquet mode $|\phi_1(t)\rangle$ with increasing drive amplitude starting from the undriven case.

This phenomenon is closely related to chaos-assisted tunneling (CAT) [26]. In CAT, tunneling between two sets of disjoint regular states is facilitated by their coupling to delocalized states in the chaotic layer. Moreover, because of the participation of states within the chaotic layer, the tunneling rates are expected to vary widely with the control parameters [26]. For the transmon, chaos can assist tunneling between different wells of the cosine potential. Because the phase of the transmon is compact, tunneling between wells distant by $\delta\phi = 2\pi n$ translates to n 2π -swings of the transmon phase or, equivalently, to quantum phase-slips of order n . The transmon states acquire their n_g -dependence through these full phase rotations [1]. In the undriven transmon, the rate of these events decreases exponentially with n for large \hbar_{eff}^{-1} .

To evaluate the phase slip rate in the presence of a drive, we compute the Fourier transform of the energy bands of the system [47]. Indeed, the Fourier components $t_n = \int_{-0.5}^{0.5} dn_g \varepsilon_1(n_g) e^{i2\pi n_g n}$ of the energy $\varepsilon_1(n_g)$ of the first excited state corresponds to the rate of phase slips of order n when the system is in the first excited state [48]. The components t_n are plotted as a function of the index n in Fig. 5(b). The inset shows the exponential suppression of t_n expected for the undriven case. In the driven case (main panel), t_n is no longer exponentially suppressed with n . Instead, it shows a long tail, indicating that the sharp features seen in Fig. 5(a) results from long-range hopping between the wells.

In cold atoms trapped in a driven optical lattice, the signatures of CAT have been observed by measuring coherent oscillations between states localized in distinct wells [49, 50]. Because the phase coordinate of the transmon is compact, tunneling oscillation between wells cannot be measured. However, phase slips (due to CAT or not) lead to a phase accumulation which depends on the gate charge n_g due to the Aharonov-Casher effect [12]. Because the gate charge is a fluctuating function of time, this results in enhanced dephasing of the transmon. The increased phase slip rate due to CAT can thus in principle be witnessed through sharp variations of the pure dephasing rate γ_ϕ associated to the transmon’s 0-1 transition, as a functions of n_g and of the drive amplitude $\tilde{\varepsilon}_d$.

Within the Floquet-Markov theory, the dephasing rates takes the form [45]

$$\gamma_\phi = A_e |2g_{0,\phi}| \sqrt{|\log \omega_{IR} t_m|} + \sum_{k \neq 0} 2S(k\omega_d) |g_{k,\phi}|^2. \quad (12)$$

The first term represents $1/f$ charge noise, while the sec-

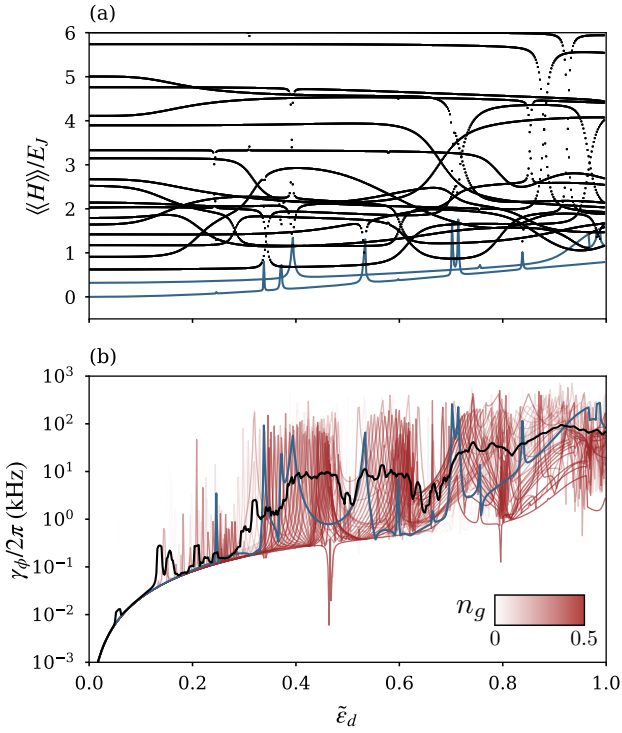


Figure 6. (a) Mean energies of Floquet states of the driven transmon as a function of the drive amplitude, with $\hbar_{\text{eff}}^{-1} = 3$, $\tilde{\omega}_d = 1.34$ and $n_g = 0.13$. While the ground and first excited states of the transmon are tracked as we vary the drive amplitude (blue lines), the rest of the states are not tracked. (b) Dephasing rate of the transmon as a function of drive amplitude due to $1/f$ charge noise and dielectric losses (see text) for 50 values of n_g distributed uniformly between 0 and 0.5 (red lines) and the same parameters used in (a). The blue line corresponds to $n_g = 0.13$, as in (a). Small resonances between the computational states and the chaotic states that can be observed in (a) result in sharp peaks in the dephasing rate, due to $1/f$ charge noise. The average dephasing rate over the offset charge (black line) is dominated by $1/f$ charge noise.

ond term comes from the possible conversion of a photon loss to a dephasing event due to the hybridization of the logical states $|0\rangle$ and $|1\rangle$. In the first term, A_e is the amplitude of charge noise, $g_{k,\phi} = n_{11k} - n_{00k}$ where n_{ijk} is a matrix element of the charge operator defined in Eq. (10), ω_{IR} is the infrared cut-off, and t_m is the characteristic measurement time. Typical values are $\sqrt{|\log \omega_{IR} t_m|} \sim 4$ and $A_e = 10^{-4}e$ [51]. In the second term, $S(\omega)$ is the spectral function of the relevant bath, here assumed to be associated to dielectric losses.

The dephasing rate obtained from Eq. (12) and the numerically obtained Floquet modes $|\phi_0(t)\rangle$ and $|\phi_1(t)\rangle$ corresponding to the logical states in the presence of a drive is shown in Fig. 6(b) as a function of $\tilde{\epsilon}_d$ for 50 values of n_g uniformly spaced in the range $[0, 0.5]$ (red lines). All curves show a slow quadratic increase of γ_ϕ with the drive amplitude due to dielectric losses through the hy-

bridization of $|0\rangle$ and $|1\rangle$ by the drive. This quadratic increase in the rate with the amplitude of the drive is a signature of a perturbative effect. More interestingly, the dephasing rate also displays sharp peaks whose position strongly depends on n_g and $\tilde{\epsilon}_d$, as is expected for CAT. To better understand the origin of these structures, the mean energy of the different Floquet mode is plotted in Fig. 6(a) for $n_g = 0.13$. The γ_ϕ obtained for the same value of the gate charge is highlighted in Fig. 6(b) (blue line). By comparing the two plots, it becomes clear that the sharp increases in γ_ϕ correspond to resonances between regular states (ground or first excited state) and chaotic states. As mentioned above, the resulting hybridization of the computational states with states that have a strong charge dispersion leads to a sharp increase in the dephasing rate. The black line is an average over all realizations of the gate charges. Depending on the time scale of the charge fluctuations [52, 53] and of time needed to measure γ_ϕ , this average may be more representative of potential experimental observations.

V. CIRCUIT QED: TRANSMON COUPLED TO A RESONATOR

We have so far treated the drive seen by the qubit as a purely classical field. To account for vacuum fluctuations and the richer structure of the energy levels, we now consider a circuit QED setup where the transmon is capacitively coupled to a cavity. In this situation, the Hamiltonian takes the form [37]

$$\begin{aligned} \mathbf{H}(t) = & 4E_C(\mathbf{n} - n_g)^2 - E_J \cos(\phi) + \varepsilon_d \cos(\omega_d t) \mathbf{n} \\ & + \omega_a \mathbf{a}^\dagger \mathbf{a} - i g \mathbf{n}(\mathbf{a} - \mathbf{a}^\dagger) \\ & - (\mathbf{a} - \mathbf{a}^\dagger) \sum_k g_k (\mathbf{b}_k - \mathbf{b}_k^\dagger) + \sum_k \omega_k \mathbf{b}_k^\dagger \mathbf{b}_k. \end{aligned} \quad (13)$$

The first row of this expression is the Hamiltonian of the driven transmon qubit, as in Eq. (2). The second row contains the free cavity Hamiltonian defined by a frequency ω_a , together with the transmon-cavity capacitive coupling g . We take $g/2\pi = 250$ MHz and $\omega_a/2\pi = 8$ GHz, with the drive detuned from the cavity at $\omega_d/2\pi = 7.5$ GHz, while keeping the same parameters for the transmon qubit as in the previous sections. Finally, the last row represents the capacitive coupling of the cavity to a bosonic bath. The drive term on the qubit can be either seen as directly acting on the qubit in the laboratory frame, or as resulting from a drive on the resonator. In that latter situation, the Hamiltonian of Eq. (13) is to be understood as expressed in a displaced frame where the drive on the cavity has been removed, i.e. $\varepsilon_d = 2g\sqrt{\bar{n}}$ where \bar{n} is the cavity steady-state photon number in the laboratory frame. In this section, we find the Floquet spectrum of Eq. (13), removing the coupling to the bath, and then calculate transition rates in linear response theory [23] (details on the Floquet simulations are provided in Appendix C).

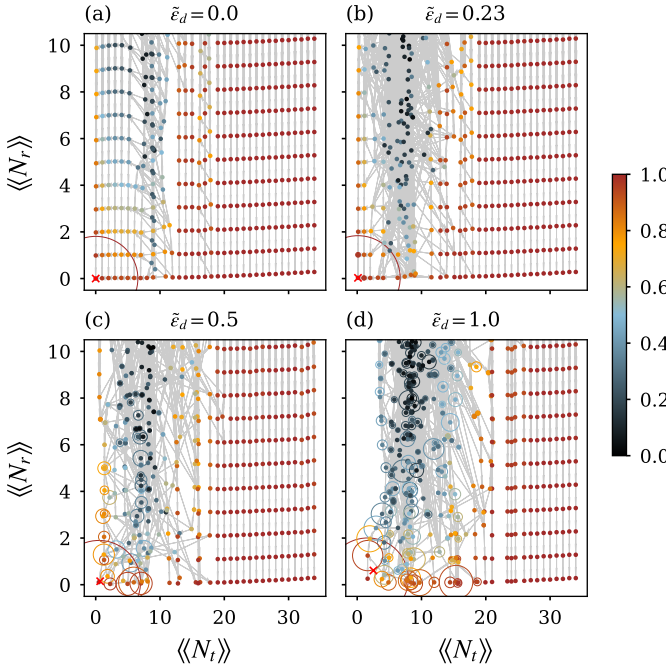


Figure 7. Grid of Floquet modes in the $(\langle N_t \rangle_t, \langle N_r \rangle_t)$ plane. The purity of the transmon reduced density matrix is encoded in the symbol color, for four different drive amplitudes: $\tilde{\varepsilon} = 0$ (a), 0.25(b), 0.5(c), and 0.95(d). In a zero-drive decoupled system, the points should form a square grid. In the coupled system, as $\langle N_r \rangle$ and $\tilde{\varepsilon}_d$ increase, level hybridization leads to grid point displacement, and purity drops. With increasing drive, for $\langle N_r \rangle_t \approx 0$, there is a purity drop in Floquet modes corresponding to the chaotic layer. Steady state of Floquet-Markov master equation is represented by a red cross. The thickness of each arrow between a pair of Floquet modes is proportional to the corresponding rate Γ_{ij} at zero temperature, apart from an offset to render the smallest rates visible. An arrow is plotted if $\Gamma_{ij} > 10^{-3} \kappa$ for (a)-(b), or $10^{-2} \kappa$ for (c)-(d). Rates of the undriven system are dominated by single-photon relaxation (vertical lines), and Purcell decay (left-to-right arrows for $\langle N_t \rangle_t \lesssim 6$) and rate flows tend to increase purity (a). Rates become increasingly non-local as the drive strength is increased (b)-(d). Steady-state populations of each Floquet mode are encoded in the radii of circles around each grid point. For sufficiently low drive the steady state is dominated by the vacuum state (a)-(c), unlike steady states above the ionization threshold (d). See Fig. 13 for the same data at higher drive power.

To characterize the structure of the Floquet spectrum, for each Floquet mode we compute expectation values of a pair of operators that are good quantum numbers in the undriven and decoupled Hamiltonian: the transmon excitation number $N_t = \sum_{i,n} i |in\rangle \langle in|$ and the resonator excitation number $N_r = \sum_{i,n} n |in\rangle \langle in|$, where $|in\rangle$ is a bare state of the joint transmon-cavity system. In Fig. 7 we show these quantities on a two-dimensional grid in the $(\langle N_t \rangle, \langle N_r \rangle)$ plane, the panels (a)-(d) representing different drive amplitudes $\tilde{\varepsilon}_d$. As in Eq. (4), the double

angle brackets represent the time-averaged expectation value of the operator in a given Floquet mode over a period of the drive. In the absence of coupling and drive, this grid is expected to be rectangular. In the coupled case, for high enough resonator photon number $\langle N_r \rangle$ or for large enough drive power, some Floquet modes deviate strongly from the regular rectangular grid. These strong deviations are associated with state dressing, and a significant hybridization of the two subsystems.

The degree of hybridization between the two subsystems is measured by the purity of the transmon reduced density matrix. Encoding this purity into the color of the grid points in Fig. 7, deviations from the rectangular grid appear to correlate with drops in purity, i.e. an increase of entanglement entropy between the transmon and the resonator. In particular, purity drops are drastic for states whose transmon excitation number corresponds to the chaotic layer identified in the previous sections for similar drive powers.

Transition rates, defined within linear response theory for the charge operator of the resonator $-i(\mathbf{a} - \mathbf{a}^\dagger)/\sqrt{2}$ as in Eq. (9), are shown as gray arrows connecting the grid points in Fig. 7. At low drive power, rates are predominantly local, consisting of single-photon relaxation (vertical downward-pointing arrows connecting neighboring grid points), and qubit Purcell decay (horizontal left-pointing arrows also connecting neighboring grid points). The existence of one dominant rate allows one to identify states corresponding to definite transmon excitation number [24, 54]. On the contrary, in the chaotic layer at finite drive amplitude the rate matrix becomes non-local connecting non-adjacent points.

Using the transition rates, we can now find the steady state of the Floquet Markov master equation [23]. In order to avoid the saturation of the resonator Hilbert space (see Appendix C), we impose a cutoff by setting all rates involving states with $\langle N_r \rangle \geq 15$ to vanish. We find that this only causes a small quantitative change in the steady-state density matrix. The transmon and resonator excitation numbers in this steady state are represented on Fig. 7 as a red cross for each drive power. Moreover, the occupation p_i of each Floquet mode in the steady state is encoded in the area of a circle centered at each grid point. For sufficiently low drive power, the steady state is dominated by the state with $\langle N_{r,t} \rangle \approx 0$, i.e. the dressed-state closest to the vacuum state. Beyond a threshold drive amplitude, the steady state of the Floquet-Markov Lindblad master equation has significant weights on the chaotic states (see Fig. 13). This threshold corresponds to transmon ionization where states above the cosine potential of the transmon become populated [13, 23, 24]. Notably, strong hybridization leads to nonzero resonator photon number in the steady state, that is $\langle N_r \rangle \gtrsim 2$ at $\tilde{\varepsilon}_d = 0.95$, see Fig. 12.

Comparing to the mean-field study of a driven transmon of the previous sections, we find that the qualitative features of the spectrum of the off-resonantly driven cir-

cuit QED Hamiltonian match those of the driven transmon qubit. To illustrate this, we plot in Fig. 8(a) the transmon excitation number $\langle\langle N_t \rangle\rangle$ for the full circuit QED model of Eq. (13) (colored dots) versus drive amplitude and compare it to the corresponding observable in the Floquet spectrum of Eq. (2) with the exact same parameters, but corresponding to a transmon driven by a classical field (black crosses). As in Fig. 7, for the former, color encodes the purity of the transmon reduced density matrix. While the agreement between the full circuit QED simulation and the mean field driven transmon is excellent for regular states, deviations appear within the chaotic layer where the purity drops. Differences within the chaotic layer between the two models are expected due to strong hybridization between the transmon and the resonator (not accounted in the mean field model), and due to fine sensitivity of chaotic spectra on external parameters [35]. Nevertheless, in the two models, the threshold values of $\tilde{\varepsilon}_d$ for the onset of chaos agree.

Lastly, performing the analog of a numerical two-tone spectroscopy experiment, in Fig. 8(b) we plot the pulled frequency response of the cavity versus drive amplitude $\tilde{\varepsilon}_d$. We first identify the cavity vacuum states corresponding to each transmon occupation number. Then, for each of these vacuum states, labeled i , we identify the transition frequency corresponding to the largest matrix element $|\mathbf{n}_{ijk}|$. The corresponding transition rate is encoded in the symbol sizes. As in Fig. 8(a), symbol colors encode the purity of the corresponding vacuum state. Only states with purity above 0.85 are plotted, for which the cavity vacuum can be well identified as the states remain close to a tensor product state.

Figure 8(b) shows that, as expected, low-energy regular states of the transmon correspond to a traceable resonator pull that is monotonically decreasing with drive strength [24, 37, 54]. In particular, there is a group of 5 levels that exhibit ac-Stark shifts monotonically evolving with drive strength $\tilde{\varepsilon}_d$ towards the bare frequency of the cavity, for sufficiently low drive. These levels correspond to resonator states pulled by the lowest regular transmon states of Fig. 8(a), and the corresponding curves terminate for drive strengths where the corresponding transmon level strongly hybridizes with the chaotic layer. The pull is vanishing for the charge-like states of the transmon, as can be identified by an inspection of the transmon excitation numbers $\langle\langle N_t \rangle\rangle$ (not shown). On the other hand, the resonator frequency pull associated with chaotic states is not shown here because the two systems strongly hybridize when the transmon is in a chaotic state, rendering impossible the identification of the resonator vacuum. Nonetheless, we address this point below when computing the steady-state density matrix.

Although it fails in the chaotic layer, perturbation theory in the transmon-cavity coupling can be used to compute the cavity pull in the regular regime, see the black symbols in Fig. 8(b). To second order, the cavity pull χ_i associated to the transmon Floquet state i is given

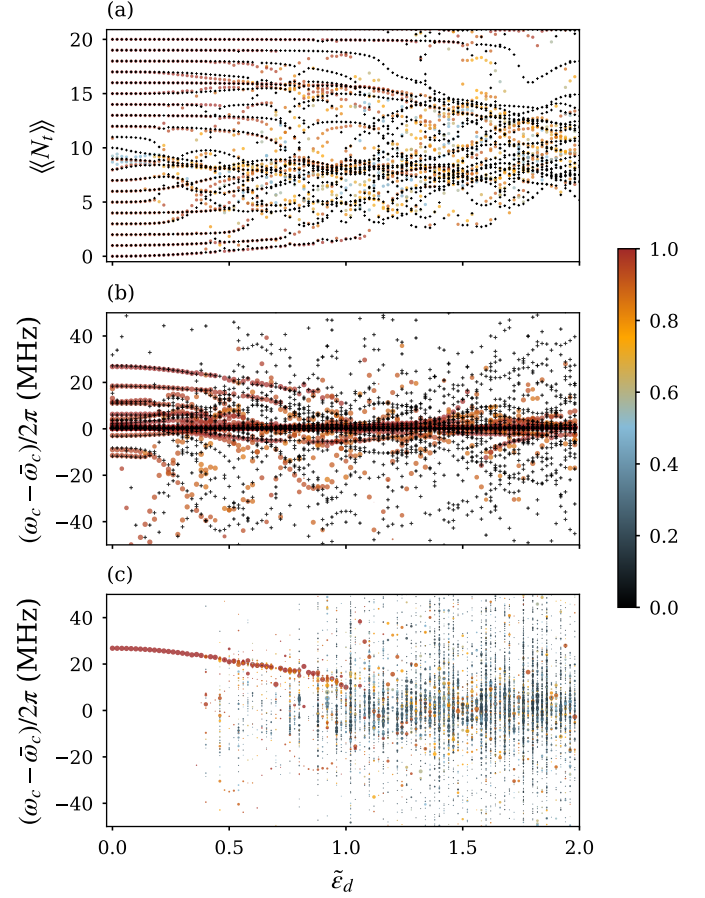


Figure 8. (a) Agreement of transmon population $\langle\langle N_t \rangle\rangle$ between the full circuit QED simulation (color encodes purity of transmon reduced density matrix; only states satisfying $\langle\langle N_r \rangle\rangle \leq 0.73$ are shown) and the driven transmon model of Eq. (2) (black crosses). (b) Pulled resonator frequency as obtained from two-tone spectroscopy, with colors representing purities of Floquet modes corresponding to the resonator vacuum (only purities above 0.85 were retained, thus excluding cavity frequency pulls due to chaotic states). Pulls from perturbation theory Eq. (14) are shown as black crosses. (c) Mean resonator frequency in the steady state. Only states where the steady-state population times the square of the transition matrix element exceeded 0.001κ .

by [55]

$$\chi_i = \sum_{j,k} g^2 n_{ijk}^2 \left(\frac{1}{\omega_a + \Delta_{ijk}} - \frac{1}{\omega_a - \Delta_{ijk}} \right), \quad (14)$$

where the charge matrix elements n_{ijk} and the energy differences Δ_{ijk} are defined in Sec. IV. For $\varepsilon_d \gg g$, n_{ijk} and Δ_{ijk} can be numerically computed by accounting for the effect of the drive on the transmon by first diagonalizing the time-dependent Hamiltonian of the driven transmon [first line of Eq. (13)], and then expressing the transmon-resonator coupling $-ig\mathbf{n}(\mathbf{a} - \mathbf{a}^\dagger)$ in the joint basis of the transmon Floquet states and cavity Fock states. In this

way, we avoid the heavy computation cost of the Floquet operator on the full transmon-cavity system. Perturbation theory (black symbols) agrees well with the full simulation only for regular states which can be identified in Fig. 8(b) by their large purity. In particular, the very good agreement between the full numerical calculations and the perturbation theory for the cavity pull of the two computational states of the transmon over the full range of drive amplitudes for which the states remain regular suggests using the Floquet basis as a starting point for perturbative treatments of multi-mode coupling used in two-qubit gate analysis [14, 56] or qubit readout [21]. This approach will be explored in future work.

Additionally, we show in Fig. 8(c) the cavity response in the steady state. For $\tilde{\varepsilon}_d \geq 0.95$ the average cavity response is centered on the bare cavity frequency, with a large variance. In [13, 23] the cavity response at the bare frequency was attributed to the Josephson potential essentially becoming transparent with strong drives. We rather observe here that this response is caused by the transmon entering a low-purity state with significant weight on a large number of chaotic Floquet modes, which corresponds to the transmon becoming strongly hybridized with the cavity and giving vanishing pull on average.

We note that the results in this section could be used to quantify to what extent the quantum non-demolition character of the light-matter interaction in Eq. (13) breaks down at high photon number or at sufficiently high drive amplitude ε_d . By quantum non-demolition, we mean that after a unitary transformation the Hamiltonian can be brought to dispersive form [37], such that in the new frame the Floquet eigenmodes become transmon-resonator tensor products. Any remaining non-QND terms in the Hamiltonian are known to affect qubit relaxation rates both within a two-level approximation of the transmon [20, 57] and in approaches assuming weak qubit anharmonicity [20, 21], based on black-box quantization [28]. In Fig. 7, those Floquet modes that have large drops in purity cannot originate from a Hamiltonian in QND form. Therefore, Fig. 7 could allow for a numerical determination of a critical photon number that marks the breakdown of the dispersive approximation [16].

VI. CONCLUSION

In summary, we have shown that the presence of classical chaos has repercussions in the driven-dissipative quantum dynamics of transmon qubits. One consequence is that part of the spectrum of the driven transmon becomes strongly correlated, i.e. it exhibits strong level hybridization, which favors chaos-assisted quantum phase slips that significantly enhance charge dispersion and qubit dephasing. This could also affect the coherence times of other Josephson-based qubits, such as the fluxonium, which involve arrays of hundreds of Josephson junctions [11, 12, 58]. However, as pointed out in

Ref. [59], the inductively shunted transmon remains stable even at large drive powers.

With full circuit QED simulations, we have also shown that states corresponding to the chaotic layer have lower purity, which indicates that perturbation theories such as the dispersive approximation [16] or black-box quantization [28] become inapplicable. In particular, for a single transmon, a Kerr nonlinear oscillator model would prove too simplistic to capture the large enhancement of charge dispersion and the strong correlations within the spectrum. This situation is analogous to recent studies of arrays of transmons [36] that show that a dispersive theory cannot reproduce the spectrum in the chaotic phase. Moreover, we show that “bright-stating” the qubit corresponds to entering a steady state that massively populates chaotic states that exhibit high hybridization with the resonator, with the resonator pull averaging to zero [13?].

This important population of the chaotic states also mean that that, in order for numerical studies to capture chaos-induced effects on the low-energy states of a single driven transmon, it is necessary to use a Hilbert space size which contains the entire chaotic layer. That is, in some instances it may be necessary to revisit the conventional wisdom that using a few transmon states is sufficient for accurate simulations of the driven transmon. Moreover, based on the study of instabilities in the classical system, it may be possible to identify favorable frequency placement for which the width of the chaotic layer is minimal, results which can be used to find optimal parameters for operations with strong drives such as dispersive qubit readout.

ACKNOWLEDGMENTS

We thank Michiel Burgelman, Mazyar Mirrahimi and Alain Sarlette for fruitful discussions. This work was supported by NSERC, the Canada First Research Excellence Fund and the U.S. Army Research Office Grant No. W911NF-18-1-0411. This material is based upon work supported by the U.S. Department of Energy, Office of Science, National Quantum Information Science Research Centers, Quantum Systems Accelerator.

Appendix A: Suppression of chaotic behavior at high-frequency driving

In Sec. III B, we study the dependence of the chaotic layer on the drive frequency. To have a fair comparison between the effects at the various frequencies, there we fix the absolute value of the ac-Stark shift of the 0 - 1 transition to 100 MHz, and correspondingly choose the drive amplitude. This is made possible by tracking the ground and first excited states to obtain the difference of the quasienergies, $\varepsilon_1 - \varepsilon_0$. The negative absolute value of the ac-Stark shift is plotted in Fig. 9 as a function of $\tilde{\varepsilon}_d$

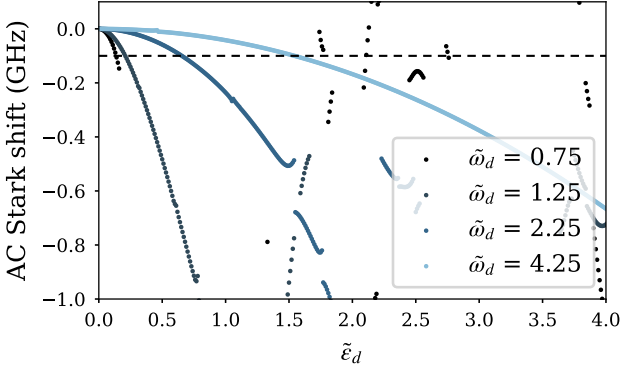


Figure 9. ac-Stark shift of the 0 - 1 transition as a function of drive amplitude $\tilde{\varepsilon}_d$, for various frequencies, and at $\hbar_{\text{eff}}^{-1} = 2.45$. The dashed line indicates an ac-Stark shift of -100MHz and the corresponding amplitudes at which the Poincaré section in Fig. 3 are plotted. Tracking is lost beyond a certain drive amplitude which is well above that needed to work at a fixed shift of -100MHz.

for various frequencies. Disruptions of the lines indicate that tracking was no longer possible.

As a complementary study to Sec. III B, in Fig. 10(a)-(d), we show the rate matrices at an ac-Stark shift of 100 MHz for the same drive frequencies. The size of the chaotic block follows that of the chaotic layer in the Poincaré sections in Fig. 3(a)-(d). In particular, the rate matrix Fig. 3(d) remains close to that of the undriven system [see inset of Fig. 4(b)], although the 0-1 transition frequency is shifted by 100 MHz.

Appendix B: Inversion symmetry sector of the driven system

In this section, we provide further explanation on the inversion symmetry discussed in Sec. IV. First, let us consider the eigenvalue equation $\mathbf{H}|\psi\rangle = E|\psi\rangle$ with \mathbf{H} the Hamiltonian Eq. (2) of the undriven transmon ($\varepsilon_d = 0$). The eigenstates of \mathbf{H} are simultaneously eigenstates of the parity operator \mathbf{P} defined as $\mathbf{P} : \mathbf{n} \rightarrow -\mathbf{n}, \phi \rightarrow -\phi$, if and only if $n_g \equiv 0, 0.5 \bmod 1$. To prove this, we define the boost operator along charge $\mathbf{U} = \exp(-in_g\phi)$. After transformation under this boost, the Hamiltonian $\mathbf{H}' = \mathbf{U}\mathbf{H}\mathbf{U}^\dagger$ does not depend on n_g and is therefore symmetric under \mathbf{P} . Thus parity acting onto an eigenstate must yield the same eigenstate if the spectrum is nondegenerate. That is, $\mathbf{P}|\psi'\rangle = e^{i\theta}|\psi'\rangle$, or $\langle -\phi|\psi'\rangle = e^{i\theta}\langle\phi|\psi'\rangle$, for all ϕ , and some phase θ independent of ϕ . Additionally, in the boosted frame, the eigenstates obey the ‘twisted-periodic’ boundary condition $\langle\phi + 2\pi|\psi'\rangle = e^{-i2\pi n_g}\langle\phi|\psi'\rangle$. Writing the two conditions above at $\phi = \pi$ gives $\langle -\pi|\psi'\rangle = e^{i\theta}\langle\pi|\psi'\rangle = e^{-i2\pi n_g}\langle\pi|\psi'\rangle$, which implies that $e^{i\theta} = e^{i2\pi n_g}$. The wavefunctions are eigenstates of parity iff $\theta = 0, \pi$, that is for $n_g = 0.0, 0.5 \bmod 1$.

As explained in the main text, in the transmon regime,

the low-energy sector is almost independent of the offset charge and the Hamiltonian becomes *effectively* parity symmetric. When parity is a symmetry of \mathbf{H} , matrix elements of the charge operator $\langle i|\mathbf{n}|j\rangle \neq 0$ iff i and j belong to different parity sectors. Therefore if $\langle i|\mathbf{n}|i\rangle \neq 0$ then parity symmetry is broken. By the Hellmann-Feynman theorem, $\langle i|\mathbf{n}|i\rangle \propto dE_i/dn_g$, so whenever a band has nonzero group velocity, parity symmetry is broken. This is why sweet spots (zero group velocity) occur at $n_g = 0, 0.5 \bmod 1$. Exponentially small group velocity, as in the transmon limit $E_J \gg E_C$, translates to exponentially weak breaking of parity. Thus, in the inset to Fig. 4(b), corresponding to $n_g = 0.25$ and thus nonzero group velocity, purple squares do appear, but they are exponentially dim. By extension, in the low-energy manifold, transitions that are forbidden by parity selection rules at $n_g = 0, 0.5 \bmod 1$ are exponentially suppressed when parity symmetry is broken, leading to an *effective* parity symmetry. Note that it is this effective symmetry in the transmon limit $E_J \gg E_C$ that allows us to ignore charge dispersion effects and express the transmon \mathbf{H} as a Kerr nonlinear oscillator.

At zero drive, this effective symmetry results in a suppression of the matrix elements of the charge operator $n_{i,i+2}$, and forbids the transition $i \rightarrow i+2$ in the low-energy sectors for both $n_g = 0.5$, where it is forbidden by a selection rule, and $n_g = 0.25$ where the effective symmetry is enforced in the transmon regime $E_J \gg E_C$. This can be seen in the rate matrices of the undriven systems – inset of Fig. 4(a,b) – where the squares corresponding to these transitions remain empty. Importantly, this symmetry is not respected at $n_g = 0.25$ for states in the separatrix region where charge dispersion become non-negligible.

In the presence of a drive $\varepsilon_d \cos(\omega_d t)\mathbf{n}$, the inversion symmetry holds if one additionally applies the operation $t \rightarrow t + \pi/\omega_d$ [31]. This symmetry of the driven Hamiltonian defines even and odd parity sectors among the time-dependent Floquet states. Note that the parity of a Floquet state depends on the Brillouin zone it belongs to in the undriven case. For example, in the undriven system, the eigenenergy of the first excited state decomposes as $E_1 = \varepsilon_1 + k\omega_d$, where the quasienergy satisfies $|\varepsilon_1| \leq \omega_d/2$, and $k = 1$ for the parameters used in Fig. 4. Within the Floquet formalism, the Floquet state, corresponding to the eigenstate $\exp(-iE_1 t)|1\rangle$ of the time evolution operator, reads $|\psi_1(t)\rangle = \exp(-i\varepsilon_1 t)|\phi_1(t)\rangle$, with the Floquet mode $|\phi_1(t)\rangle = \exp(-i\omega_d t)|1\rangle$. Since the Floquet mode $|\phi_1(t)\rangle$ is invariant under the transformation $t \rightarrow t + \pi/\omega_d$ and $\mathbf{n} \rightarrow -\mathbf{n}$, it belongs to the even sector. When increasing the drive, the state $|\phi_1(t)\rangle$ will remain in the even sector, and expands only on even states $e^{-i(2k+1)\omega_d t}|2n+1\rangle, e^{-i2k\omega_d t}|2n\rangle$, with $k \in \mathbb{Z}$ and $n \in \mathbb{N}$.

Under this symmetry, transitions through the charge operator between two states of the same (opposite) parity can only involve an odd (even) number of drive photons k , as the charge operator already changes the parity. This results in superposition of blue and red squares in at $n_g =$

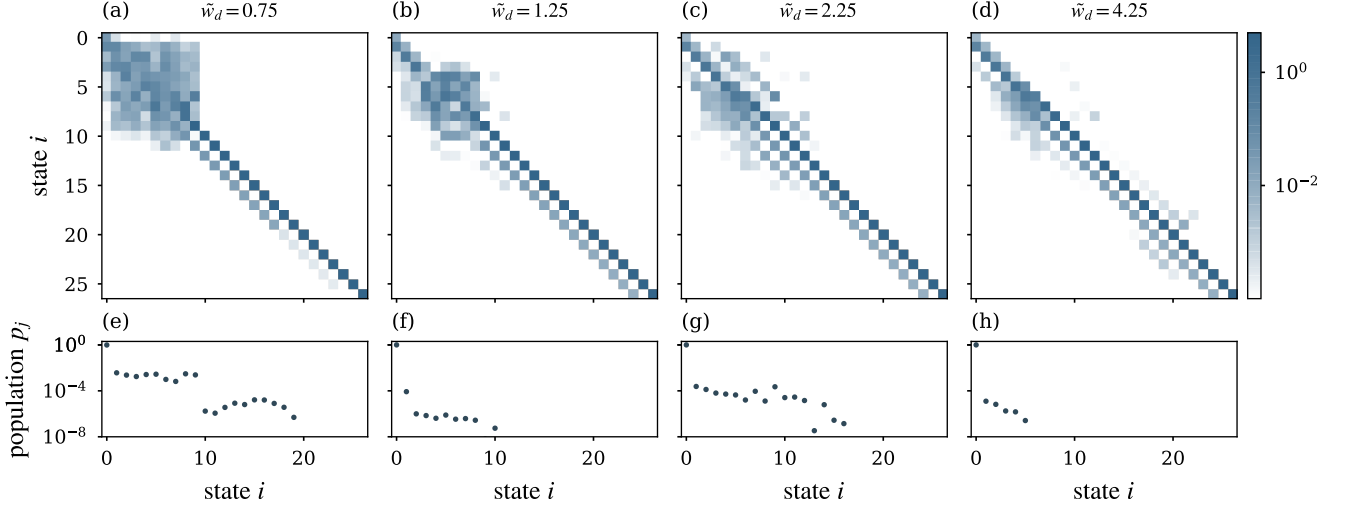


Figure 10. Rate matrices and steady-state populations at for the same parameters as in Fig. 3, with the drive amplitude corresponding to an ac-Stark shift of -100MHz . The rate matrices (b) and (d) are more regular, resulting in a smaller plateau in the steady-state distribution.

0.5 (see Fig. 4(a)). On the contrary, at $n_g = 0.25$, purple squares, indicative of red and blue contributions, light up not only in the chaotic block, but also for transitions involving the low-energy states.

Transitions which do not respect the apparent symmetry of the transmon were experimentally observed in Sank *et al.* [22] but remained unexplained. There, the situation is slightly more complicated as a harmonic mode is capacitively coupled to the transmon, making this effectively a 3-mode problem. Nonetheless, the situation is similar, and the same conclusions can be drawn. Indeed, the inversion symmetry for the full Hamiltonian holds upon adding the transformation $\mathbf{n}_r \rightarrow -\mathbf{n}_r$, where $\mathbf{n}_r = -i(\mathbf{a} - \mathbf{a}^\dagger)/\sqrt{2}$ is the charge operator of the resonator. Because the resonator is low-Q, transitions between states are most likely to be induced by the bath coupled to the resonator through the resonator charge operator \mathbf{n}_r . Since \mathbf{n}_r maps one parity sector to another similarly to \mathbf{n} , the single driven transmon analysis remains valid for the full driven circuit QED setup.

Appendix C: Floquet simulations for circuit QED Hamiltonian

In this Appendix, we provide more details for the numerical simulations presented in Sec. V. To capture the entirety of the chaotic layer even at strong drives $\tilde{\varepsilon}_d \geq 1$, we have used a local Hilbert space size of 35 for the transmon. For the resonator, we use 20 states, which is pertinent in the regime of off-resonant drives (here, the drive frequency is 500 MHz below the bare cavity frequency at 8 GHz). We characterize truncation errors by plotting the error in the bosonic commutation relation in Fig. 11, and observe significant errors of the commutator only for

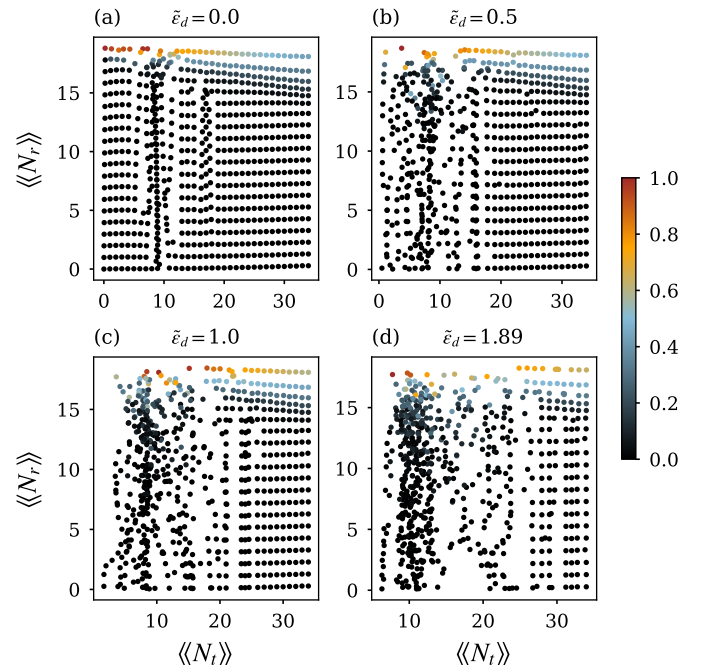


Figure 11. Commutator error, encoded in symbol color, for each Floquet mode, expressed as $|1 - \langle\langle [\mathbf{a}, \mathbf{a}^\dagger] \rangle\rangle|$.

states with $\langle\langle N_r \rangle\rangle \geq 12$. We also observe a ‘reflection’ at the Hilbert space boundary [?], as indicated by monotonically decreasing values of $\langle\langle N_r \rangle\rangle$ versus $\langle\langle N_t \rangle\rangle$ (upper regions of the four panels of Fig. 11).

Boundary effects in the Hilbert space become important at strong drives, where states with high $\langle\langle N_r \rangle\rangle$ become populated, see Fig. 12. In particular, averaging

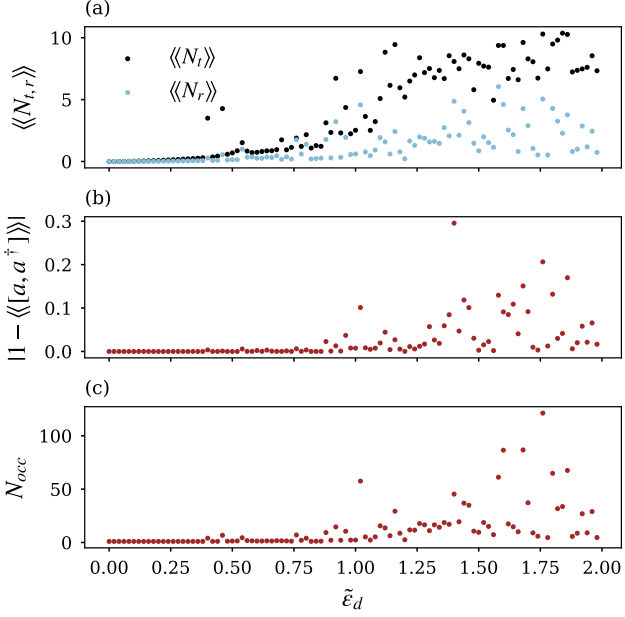


Figure 12. (a) Steady state population of the transmon and resonator as a function of drive strength. Both expectation values become non-monotonic beyond a threshold at $\tilde{\epsilon}_d \simeq 1$. (b) Commutator error (see also Fig. 11) in the steady state. (c) Number of occupied Floquet modes in the steady state [59] as calculated from the entanglement entropy $N_{occ} = \exp(-\sum_i p_i \log p_i)$.

the commutator error in the steady state of the driven-dissipative evolution, we find that it correlates well with the number of occupied Floquet modes as determined from the entanglement entropy of the steady-state density matrix [59] [Fig. 12(b) and (c)], which occurs at about the same threshold power $\tilde{\epsilon}$ as ionization, defined as a significant increase in $\langle\langle N_t \rangle\rangle$ Fig. 12(a).

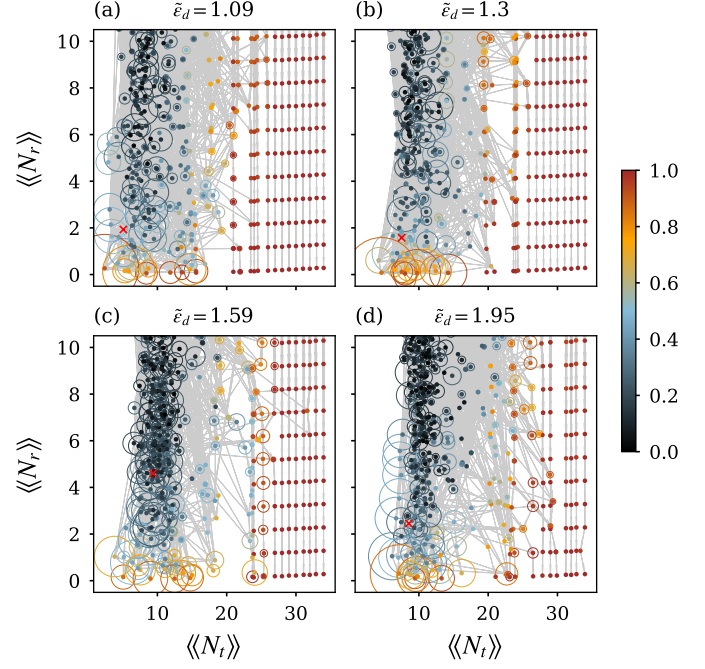


Figure 13. Same as Fig. 7, but for higher drive strengths. Steady-state expectation values of resonator photon number and transmon excitation number deviate significantly from zero. The steady state has significant weight over a large number of chaotic states. An arrow is plotted if $\Gamma_{ij} > 10^{-3} \kappa$ for (a)-(b), or $10^{-2} \kappa$ for (c)-(d).

[1] J. Koch, T. M. Yu, J. Gambetta, A. A. Houck, D. I. Schuster, J. Majer, A. Blais, M. H. Devoret, S. M. Girvin, and R. J. Schoelkopf, *Physical Review A* **76**, 042319 (2007).

[2] N. Earnest, S. Chakram, Y. Lu, N. Irons, R. Naik, N. Leung, L. Ocola, D. Czaplewski, B. Baker, J. Lawrence, J. Koch, and D. Schuster, *Physical Review Letters* **120**, 150504 (2018).

[3] Y.-H. Lin, L. B. Nguyen, N. Grabon, J. San Miguel, N. Pankratova, and V. E. Manucharyan, *Physical Review Letters* **120**, 150503 (2018).

[4] A. Gynis, P. S. Mundada, A. Di Paolo, T. M. Hazard, X. You, D. I. Schuster, J. Koch, A. Blais, and A. A. Houck, *PRX Quantum* **2**, 010339 (2021).

[5] J. Q. You, X. Hu, S. Ashhab, and F. Nori, *Phys. Rev. B* **75**, 140515 (2007).

[6] F. Yan, S. Gustavsson, A. Kamal, J. Birenbaum, A. P. Sears, D. Hover, T. J. Gudmundsen, D. Rosenberg, G. Samach, S. Weber, J. L. Yoder, T. P. Orlando, J. Clarke, A. J. Kerman, and W. D. Oliver, *Nature Communications* **7**, 12964 (2016).

[7] M. Mirrahimi, Z. Leghtas, V. V. Albert, S. Touzard, R. J. Schoelkopf, L. Jiang, and M. H. Devoret, *New Journal of Physics* **16**, 045014 (2014).

[8] Z. Leghtas, S. Touzard, I. M. Pop, A. Kou, B. Vlastakis, A. Petrenko, K. M. Sliwa, A. Narla, S. Shankar, M. J. Hatridge, M. Reagor, L. Frunzio, R. J. Schoelkopf, M. Mirrahimi, and M. H. Devoret, *Science* **347**, 853 (2015), <https://www.science.org/doi/pdf/10.1126/science.aaa2085>.

[9] R. Lescanne, M. Villiers, T. Peronnin, A. Sarlette, M. Delbecq, B. Huard, T. Kontos, M. Mirrahimi, and Z. Leghtas, *Nature Physics* **16**, 509 (2020).

[10] V. Sivak, N. Frattini, V. Joshi, A. Lingenfelter, S. Shankar, and M. Devoret, *Physical Review Applied* **11**, 054060 (2019).

[11] N. A. Masluk, I. M. Pop, A. Kamal, Z. K. Minev, and M. H. Devoret, *Physical Review Letters* **109**, 137002 (2012).

[12] V. E. Manucharyan, N. A. Masluk, A. Kamal, J. Koch, L. I. Glazman, and M. H. Devoret, *Physical Review B* **85**, 024521 (2012).

[13] R. Lescanne, L. Verney, Q. Ficheux, M. H. Devoret, B. Huard, M. Mirrahimi, and Z. Leghtas, *Physical Review Applied* **11**, 014030 (2019).

[14] S. Sheldon, E. Magesan, J. M. Chow, and J. M. Gambetta, *Physical Review A* **93**, 060302 (2016), arXiv: 1603.04821.

[15] H. Paik, A. Mezzacapo, M. Sandberg, D. T. McClure, B. Abdo, A. D. Córcoles, O. Dial, D. F. Bogorin, B. L. T. Plourde, M. Steffen, A. W. Cross, J. M. Gambetta, and J. M. Chow, *Phys. Rev. Lett.* **117**, 250502 (2016).

[16] A. Blais, R.-S. Huang, A. Wallraff, S. M. Girvin, and R. J. Schoelkopf, *Physical Review A* **69** (2004), 10.1103/physreva.69.062320.

[17] T. Walter, P. Kurpiers, S. Gasparinetti, P. Magnard, A. Potočnik, Y. Salathé, M. Pechal, M. Mondal, M. Oppliger, C. Eichler, and A. Wallraff, *Physical Review Applied* **7**, 054020 (2017).

[18] Z. Minev, S. Mundhada, S. Shankar, P. Reinhold, R. Gutiérrez-Jáuregui, R. Schoelkopf, M. Mirrahimi, H. Carmichael, and M. Devoret, *Nature* **570**, 200 (2019).

[19] A. Grimm, N. E. Frattini, S. Puri, S. O. Mundhada, S. Touzard, M. Mirrahimi, S. M. Girvin, S. Shankar, and M. H. Devoret, *Nature* **584**, 205 (2020).

[20] M. Boissonneault, J. M. Gambetta, and A. Blais, *Physical Review A* **79**, 013819 (2009); M. Malekakhlagh, A. Petrescu, and H. E. Türeci, *Phys. Rev. B* **101**, 134509 (2020).

[21] A. Petrescu, M. Malekakhlagh, and H. E. Türeci, *Phys. Rev. B* **101**, 134510 (2020).

[22] D. Sank, Z. Chen, M. Khezri, J. Kelly, R. Barends, B. Campbell, Y. Chen, B. Chiaro, A. Dunsworth, A. Fowler, E. Jeffrey, E. Lucero, A. Megrant, J. Mutus, M. Neeley, C. Neill, P. O’Malley, C. Quintana, P. Roushan, A. Vainsencher, T. White, J. Wenner, A. N. Korotkov, and J. M. Martinis, *Physical Review Letters* **117**, 190503 (2016).

[23] L. Verney, R. Lescanne, M. H. Devoret, Z. Leghtas, and M. Mirrahimi, *Phys. Rev. Applied* **11**, 024003 (2019).

[24] R. Shillito, A. Petrescu, J. Cohen, J. Beall, M. Hauru, M. Ganahl, A. G. M. Lewis, G. Vidal, and A. Blais, “Dynamics of transmon ionization,” (2022).

[25] T. Walter, P. Kurpiers, S. Gasparinetti, P. Magnard, A. Potočnik, Y. Salathé, M. Pechal, M. Mondal, M. Oppliger, C. Eichler, and A. Wallraff, *Phys. Rev. Applied* **7**, 054020 (2017).

[26] S. Tomsovic and D. Ullmo, *Physical Review E* **50**, 145 (1994).

[27] K. A. Matveev, A. I. Larkin, and L. I. Glazman, *Phys. Rev. Lett.* **89**, 096802 (2002).

[28] S. E. Nigg, H. Paik, B. Vlastakis, G. Kirchmair, S. Shankar, L. Frunzio, M. H. Devoret, R. J. Schoelkopf, and S. M. Girvin, *Physical Review Letters* **108** (2012), 10.1103/physrevlett.108.240502.

[29] H.-P. Breuer, W. Huber, and F. Petruccione, *Physical Review E* **61**, 4883 (2000).

[30] R. Ketzmerick and W. Wustmann, *Physical Review E* **82**, 021114 (2010).

[31] M. Grifoni and P. Hänggi, *Physics Reports* **304**, 229 (1998).

[32] B. V. Chirikov, *Physics Reports* **52**, 263 (1979).

[33] I. C. Percival, *Journal of Physics B: Atomic and Molecular Physics* **6**, L229 (1973).

[34] M. V. Berry, *Journal of Physics A: Math. Gen.* **10**, 2083 (1977).

[35] F. Haake, *Quantum Signatures of Chaos* (Springer, Berlin, Germany, 2010).

[36] C. Berke, E. Varvelis, S. Trebst, A. Altland, and D. P. DiVincenzo, *Nat. Commun.* **13**, 1 (2022).

[37] A. Blais, A. L. Grimsmo, S. M. Girvin, and A. Wallraff, *Rev. Mod. Phys.* **93**, 025005 (2021).

[38] G. M. Zaslavskii, R. Z. Sagdeev, D. A. Usikov, and A. A. Chernikov, *Weak Chaos and Quasi-Regular Patterns*, edited by A. R. Sagdeeva, Cambridge Nonlinear Science Series (Cambridge University Press, 1991).

[39] R. Ketzmerick and W. Wustmann, *Phys. Rev. E* **82**, 021114 (2010).

[40] A. Bäcker, R. Ketzmerick, S. Löck, and L. Schilling, *Physical Review Letters* **100**, 104101 (2008).

[41] R. Graham, *Europhysics Letters (EPL)* **7**, 671 (1988).

[42] J. A. González and M. A. del Olmo, *Journal of Physics A: Mathematical and General* **31**, 8841 (1998).

[43] M. L. Mehta, *Random Matrices*, revised and enlarged 2nd ed., edited by M. L. Mehta (Academic Press, San Diego, 1991) pp. 1–35.

[44] N. Bubner and R. Graham, Physical Review A **43**, 1783 (1991).

[45] Z. Huang, P. S. Mundada, A. Gyenis, D. I. Schuster, A. A. Houck, and J. Koch, arXiv:2004.12458 [quant-ph] (2020), arXiv: 2004.12458.

[46] S. material, .

[47] M. Martinez, O. Giraud, D. Ullmo, J. Billy, D. Guéry-Odelin, B. Georgeot, and G. Lemarié, Physical Review Letters **126**, 174102 (2021).

[48] J. Koch, V. Manucharyan, M. H. Devoret, and L. I. Glazman, Physical Review Letters **103**, 217004 (2009).

[49] A. Mouchet, C. Miniatura, R. Kaiser, B. Grémaud, and D. Delande, Physical Review E **64**, 016221 (2001), arXiv: nlin/0012013.

[50] M. Arnal, G. Chatelain, M. Martinez, N. Dupont, O. Giraud, D. Ullmo, B. Georgeot, G. Lemarié, J. Billy, and D. Guéry-Odelin, Science Advances **6**, eabc4886 (2020), <https://www.science.org/doi/pdf/10.1126/sciadv.abc4886>.

[51] G. Ithier, E. Collin, P. Joyez, P. J. Meeson, D. Vion, D. Esteve, F. Chiarello, A. Shnirman, Y. Makhlin, J. Schriefl, and G. Schön, Phys. Rev. B **72**, 134519 (2005).

[52] B. G. Christensen, C. D. Wilen, A. Opremcak, J. Nelson, F. Schlenker, C. H. Zimonick, L. Faoro, L. B. Ioffe, Y. J. Rosen, J. L. DuBois, B. L. T. Plourde, and R. McDermott, Phys. Rev. B **100**, 140503 (2019).

[53] C. D. Wilen, S. Abdullah, N. A. Kurinsky, C. Stanford, L. Cardani, G. D’Imperio, C. Tomei, L. Faoro, L. B. Ioffe, C. H. Liu, A. Opremcak, B. G. Christensen, J. L. DuBois, and R. McDermott, Nature **594**, 369 (2021).

[54] M. Boissonneault, J. M. Gambetta, and A. Blais, Phys. Rev. Lett. **105**, 100504 (2010).

[55] V. Gramich, S. Gasparinetti, P. Solinas, and J. Ankerhold, Physical Review Letters **113**, 027001 (2014).

[56] M. Malekakhlagh, Physical Review A , 28 (2020).

[57] E. A. Sete, J. M. Gambetta, and A. N. Korotkov, Phys. Rev. B **89**, 104516 (2014).

[58] L. B. Nguyen, Y.-H. Lin, A. Somoroff, R. Mencia, N. Grabon, and V. E. Manucharyan, Physical Review X **9**, 041041 (2019).

[59] M. Burgelman, P. Rouchon, A. Sarlette, and M. Mirrahimi, “Structurally stable subharmonic regime of a driven quantum josephson circuit,” (2022).